SERDP

TECHNICAL REPORT

Meshfree Modeling of Munitions Penetration in Soils

Year 2 Progress Report

Sheng-Wei Chi
University of Illinois at Chicago

October 2020

SERDP Project MR-2628

REPORT DOCUMENTATION PAGE

Form Approved
OMB No. 0704-0188

1. REPORT DATE *(DD-MM-YYYY)*	**2. REPORT TYPE**	**3. DATES COVERED** *(From - To)*
31/10/2020	SERDP Technical Report	9/28/2018 - 9/28/2021

4. TITLE AND SUBTITLE

Meshfree Modeling of Munitions Penetration in Soils

Year 2 Progress Report

5a. CONTRACT NUMBER
18-C-0099

5b. GRANT NUMBER

5c. PROGRAM ELEMENT NUMBER

6. AUTHOR(S)
Sheng-Wei Chi

5d. PROJECT NUMBER
MR-2628

5e. TASK NUMBER

5f. WORK UNIT NUMBER

7. PERFORMING ORGANIZATION NAME(S) AND ADDRESS(ES)
University of Illinois at Chicago
Civil and Materials Engineering
842 W. Taylor Street
3087 Engineering Research Facility
Chicago, IL 60607-7023

8. PERFORMING ORGANIZATION REPORT NUMBER
MR-2628

9. SPONSORING/MONITORING AGENCY NAME(S) AND ADDRESS(ES)
Strategic Environmental Research and Development Program
4800 Mark Center Drive, Suite 16F16
Alexandria, VA 22350-3605

10. SPONSOR/MONITOR'S ACRONYM(S)
SERDP

11. SPONSOR/MONITOR'S REPORT NUMBER(S)
MR-2628

12. DISTRIBUTION/AVAILABILITY STATEMENT
DISTRIBUTION STATEMENT A. Approved for public release: distribution unlimited.

13. SUPPLEMENTARY NOTES

14. ABSTRACT
The objective of this project is to develop physics-based models to predict the penetration depth of common military munitions in various soil conditions. Ultimately, the models will be used to determine probable depths of munitions in the soil of formerly used defense sites in support of planning for remediation. The simulation results can be used to aid sensor detection and removal of these munitions.

15. SUBJECT TERMS
Meshfree Modeling, Munitions Penetration, Soils, munitions response, UXO, UXO on land, impact burial

16. SECURITY CLASSIFICATION OF:			**17. LIMITATION OF ABSTRACT**	**18. NUMBER OF PAGES**	**19a. NAME OF RESPONSIBLE PERSON**
a. REPORT	**b. ABSTRACT**	**c. THIS PAGE**			Sheng-Wei Chi
UNCLASS	UNCLASS	UNCLASS	UNCLASS	55	**19b. TELEPHONE NUMBER** *(Include area code)* 312-996-5024

Table of Contents

List of Tables

List of Figures

Meshfree Modeling of Munitions Penetration in Soils

Sheng-Wei Chi, Craig Foster, Mohammed Atif, Xuejun Li, and Jianfei Tian

Department of Civil, Materials, and Environmental Engineering
University of Illinois at Chicago, Chicago, IL 60607
swchi@uic.edu

1. Project Objective

The objective of this project is to develop physics-based models to predict the penetration depth of common military munitions in various soil conditions. Ultimately, the models will be used to determine probable depths of munitions in the soil of formerly used defense sites in support of planning for remediation. The simulation results can be used to aid sensor detection and removal of these munitions.

2. Summary of Outcomes in the Reporting Year

- A novel domain integration, termed as MPIM, for the Galerkin-based meshfree method was developed and its performance was verified by several benchmarks. The MPIM provides stable and accurate solutions in the semi-Lagrangian Reproducing Kernel formulation. The numerical solutions show that the MPIM is more effective than existing methods for the meshfree simulation of penetration into soil.
- A rigorous strategy for calibration of parameters in the three-invariant soil model was developed. The procedure was verified by calibrating the required soil parameters from the experimental data in the literature.
- The Sobol variance-based sensitivity analysis was conducted to identify the key parameters in the three-invariant soil model. The initial yield stress, the initial shear strength, the shear yield surface parameter, and Young's modulus have significant influences on the outputs of designed simulations.
- A partially saturated soil model was developed and implemented. It was extended from the Biot mixture theory. Several benchmarks were utilized to verify the developed model.
- A penetration test apparatus was built in the High-Bay Structures Lab at the UIC. The apparatus was designed to launch a steel ball of 1" diameter at a velocity of 120 m/s. The apparatus will be used to conduct penetration tests of soil under different saturation conditions.
- Soil tests for fully saturated silica sand were conducted and the soil properties were calibrated. The test data will be used to validate the numerical model.
- The experiment of an ogive bullet penetrating coarse sand in Hankins et al. (2006) was simulated to validate the updated meshfree code. The numerical predictions for impact velocities ranging from 20 m/s to 170 m/s show a trend that agrees with the experimental data.

- Journal paper publication:
    - Mahdavi, A., Chi, S.W., and Atif, M.M., "A two-field semi-Lagrangian reproducing kernel model for impact and penetration simulation into geo-materials," Computational Particle Mechanics, 7, p. 351–364 (2020)

3. Tasks Accomplished

3.1. Enhancement of Multi-field Meshfree Implementation

3.1.1. Midpoint Integration Method

In the meshfree formulation used in this project, namely semi-Lagrangian Reproducing Kernel formulation (Chi et al., 2015), the approximate solution is obtained based on the Galerkin formulation, where the integration over the entire domain is required. Despite efforts made over the past two decades, domain integration remains a challenge in Galerkin-based meshfree methods due to instability and sub-optimal convergence. Although background cell integration with a high order quadrature rule can achieve convergence and stability, it requires the integration mesh for quadrature points and becomes computationally inefficient in the semi-Lagrangian formulation.

While a node-based integration scheme, such as direct nodal integration (DNI), is desired in the meshfree methods since it can naturally cope with the point-based approximation and offer simplicity and computational efficiency, it suffers from instability and low convergence rates. Several nodal integrations were developed to alleviate the abovementioned drawbacks. Chen et al. (2001) introduced the stabilized conforming nodal integration (SCNI) to achieve optimal convergence and remove spurious zero-energy modes due to nodal integration. Since constructing conforming integration cells is almost infeasible in the semi-Lagrangian formulation, a non-conforming version of SCNI, termed as stabilized non-conforming nodal integration (SNNI), was later proposed (Chen and Wu, 2007). Nonetheless, spurious, oscillatory low-energy modes still exist in both SCNI and SNNI and cause instability. Additional stabilization terms were introduced to further remove the low-energy spurious modes, resulting in modified SCNI (MSCNI) and SNNI (MSNNI) (Chen et al., 2007). Chen et al. (2014) introduced a variationally consistent integration (VCI) to restore the desired order of exactness for any numerical integration schemes in the Galerkin formulation and achieve the optimal convergence. Hillman and Chen (2016) introduced the naturally stabilized nodal integration (NSNI) to eliminate the spurious low energy modes in direct nodal integration with a tunable parameter. Although a combination of NSNI with VCI maintains optimal convergence and stability, the requirement of contour integration in the VCI posts a major challenge in meshfree simulations involving contact and materials separation. A novel domain integration method, termed as midpoint integration method (MPIM), is developed to achieve both accuracy and stability for extremely large deformation analyses. The MPIM is derived based on the modified Simpson's rule. It needs neither conforming integration cells nor contour integrals to ensure accuracy and stability, while the resultant discrete system is symmetric and thus the momentum conservation is preserved.

The schematic of the integration subdomain associated with a meshfree node in the MPIM is illustrated in Figure 1, where a one-dimensional domain is discretized non-uniformly and the midpoint, node, and evaluation points are depicted. The modified Simpson's rule for the integration of a function f within $\Delta x = \Delta x_1 + \Delta x_2$, which is sixth-order accurate, can be expressed as follows.

$$\int_{x-\Delta x_1}^{x-\Delta x_2} f\,dx = \left(\frac{7f(x-\Delta x_1)+16f(x_m)+7f(x-\Delta x_2)}{30}\right)\Delta x - \left(\frac{f'(x-\Delta x_2)-f'(x-\Delta x_1)}{60}\right)\Delta x^2 + O(\Delta x^6) \tag{1}$$

where x_m is the middle point of the subdomain, and Δx is the length of the subdomain.

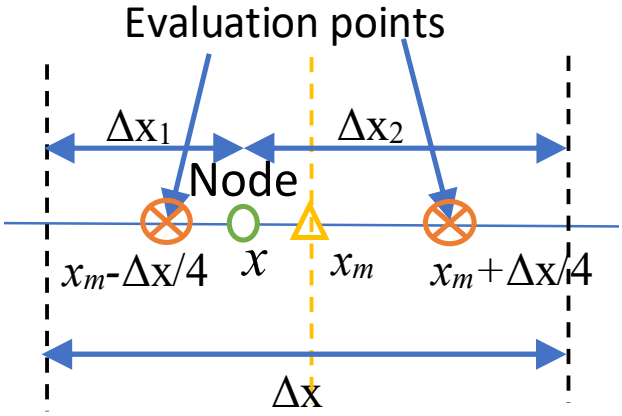

Figure 1. Schematic of the node subdomain

The modified Simpson's rule is derived based on a conforming mesh, which becomes computationally very expensive in the penetration simulations. To overcome the above issue, a midpoint integration method (MPIM) is developed without conforming integration subdomains. It is designed to achieve the optimal integration accuracy using only evaluation points that are at an equal distance from the midpoint of the subdomain. The MPIM in one dimension is given as follows and can be shown to achieve the accuracy of 4th order with a non-uniform mesh.

$$\int_{x-\Delta x_1}^{x-\Delta x_2} f\,dx = \left(\frac{f(x_m-\Delta x/4)+f(x_m+\Delta x/4)}{2}\right)\Delta x + \left(\frac{f'(x_m+\Delta x/4)-f'(x_m-\Delta x/4)}{48}\right)\Delta x^2 + O(\Delta x^4) \tag{2}$$

The MPIM can be extended for two and three dimensions using the tensor product. Figure 2 illustrates the integration subdomains, a rectangle for 2D and a cuboid for 3D, around the midpoint. The corner points are selected as the evaluation points. For 2D, the midpoint integration rule is calculated as:

$$\iint f dxdy \approx \left(\sum_{I=1}^{4} f(x_I) / 4 \right) \iint dxdy + g_x ml_x + g_y ml_y \ , \qquad (3)$$

where ml_x, ml_y are derived to achieve desired accuracy (Cerone et al. 2006). In this study, $ml_x = \Delta x \, A / 96$ and $ml_y = \Delta y \, A / 96$ with $A = \iint dxdy$ are derived and $g_x = \sum_{I=1}^{4} \tilde{N}_x f(x_I) n_x$ $g_y = \sum_{I=1}^{4} \tilde{N}_y f(x_I) n_y$ with n_x and n_y the x- and y- components of the outward unit normal, respectively. Similarly, for 3D, the midpoint integration rule is calculated as:

$$\iiint f \ dxdydz \approx \left(\sum_{i=1}^{8} f(x_i) / 8 \right) \iiint dxdydz + g_x ml_x + g_y ml_y + g_z ml_z \qquad (4)$$

Above $ml_x = \Delta x \, V / 192$, $ml_y = \Delta y \, V / 192$, and $ml_z = \Delta z \, V / 192$ with $V = \iiint dxdydz$ are derived and $g_x = \sum_{I=1}^{8} \tilde{N}_x f(x_I) n_x$, $g_y = \sum_{I=1}^{8} \tilde{N}_y f(x_I) n_y$, and $g_z = \sum_{I=1}^{8} \tilde{N}_z f(x_I) n_z$. As a result, the MPIM approximates the domain integration of a function around the midpoint of the subdomain created at an initial configuration. One of the advantages of the method is that it does not require VCI correction, which is not straightforward to obtain when dealing with continuous evolving surfaces, to attain the desired convergence.

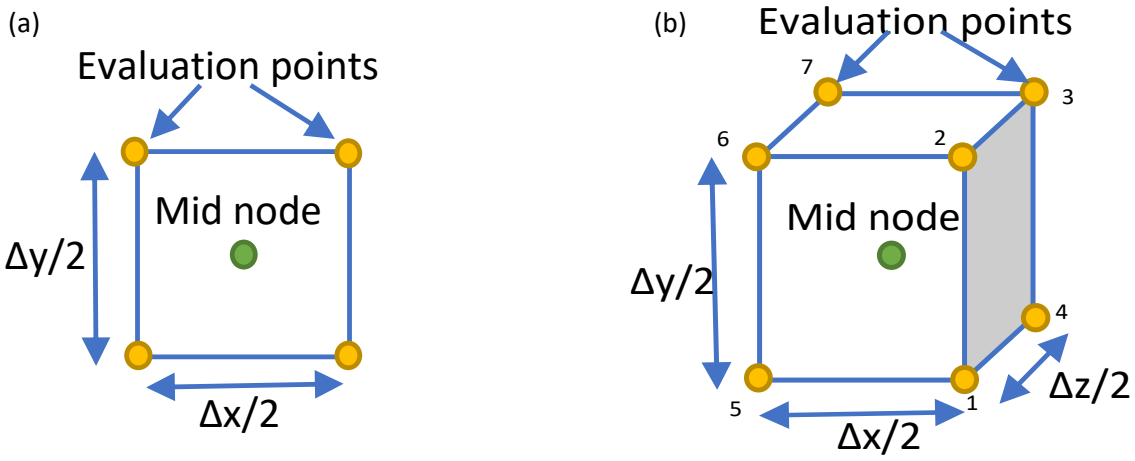

Figure 2. Schematic of integration subdomain and evaluation points in MPIM for (a) 2D and (b) 3D

3.1.2. Verification of Midpoint Integration Method

The performance of the newly derived MPIM is examined using several benchmarks and compared with existing integration techniques before applied to the penetration simulations.

3.1.2.1. Eigen Analysis

An eigenvalue analysis is employed to assess the stability of the MPIM. The stiffness matrix of a 1D elastic rod discretized into 200 nodes is obtained and its eigenvalues and eigenmodes are examined. The results by MPIM are compared with those by DNI, SCNI, 5-point Gauss integration, and Finite Element Method (FEM) in Figure 3. As can be seen in Figure 3a, the spectrum of the MPIM is comparable to and slightly higher than those of 5-point Gauss integration and fully integration FEM. Moreover, no spurious, oscillatory eigenmodes are observed in the MPIM whereas the well-known SCNI method exhibits a spurious mode associated with the ninth-lowest eigenvalues (Figure 3b).

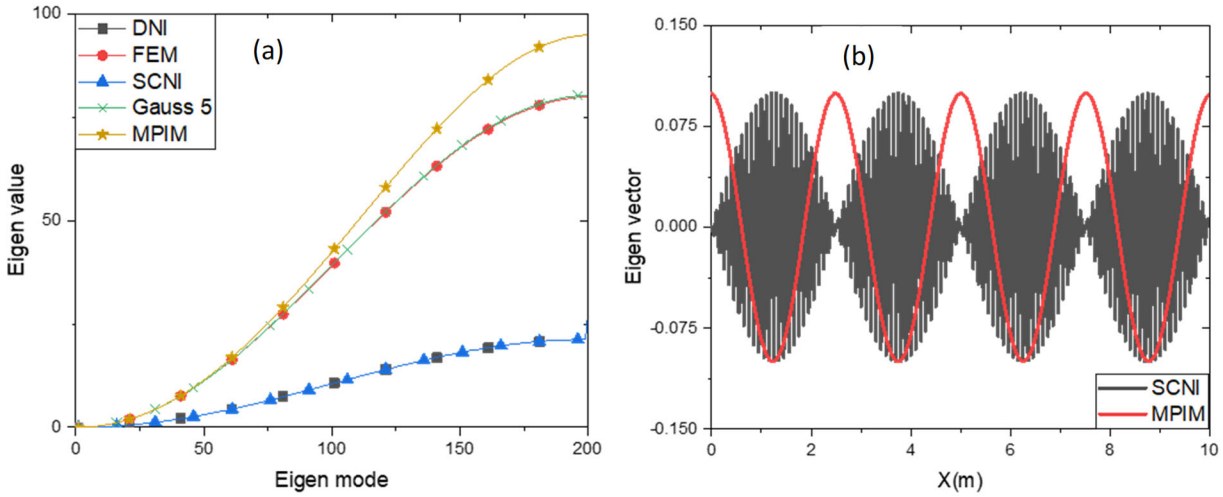

Figure 3. (a) eigen spectrum and (b) mode shape of the 9th mode

3.1.2.2. Elastic Wave Propagation

The 1D wave propagation in an elastic bar of length L=5.0 m with an initial velocity of 30 m/s is analyzed to examine the performance of the MPIM in the semi-Lagrangian formulation as illustrated in Figure 4. The material properties of the elastic bar are Young's modulus = 40 MPa and density = 2000 kg/m^3. The semi-Lagrangian RK with a normalized support size of 2.0 is considered for the problem. The domain is discretized uniformly with 21 nodes and an explicit temporal integration is employed for the numerical solution. The numerical solutions are compared with domain integration schemes from SNNI, NSNI, and NSNI+VCI. The reference solution is obtained by using 9-point Gauss integration in the Lagrangian formulation.

From Figure 5, it is observed that the SNNI solution becomes unstable whereas the NSNI solution yields a large error in the amplitude and phase when the wave propagates. On the other hand, NSNI+VCI and MPIM both provide accurate solutions at first glance. On a closer inspection in Figure 5c, it can be observed that the MPIM yields lower error when compared with the NSNI+VCI. The MPIM achieves stable and accurate solutions without additional integration correction when compared with other methods.

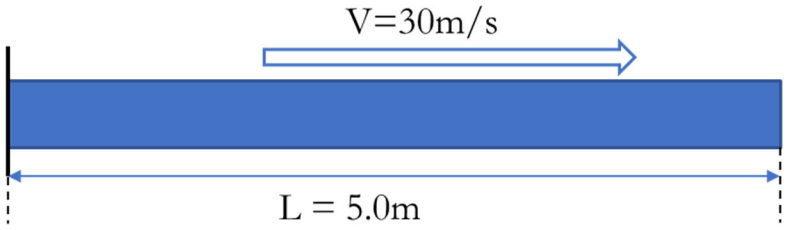

Figure 4. Schematic of a linear elastic bar with an initial velocity

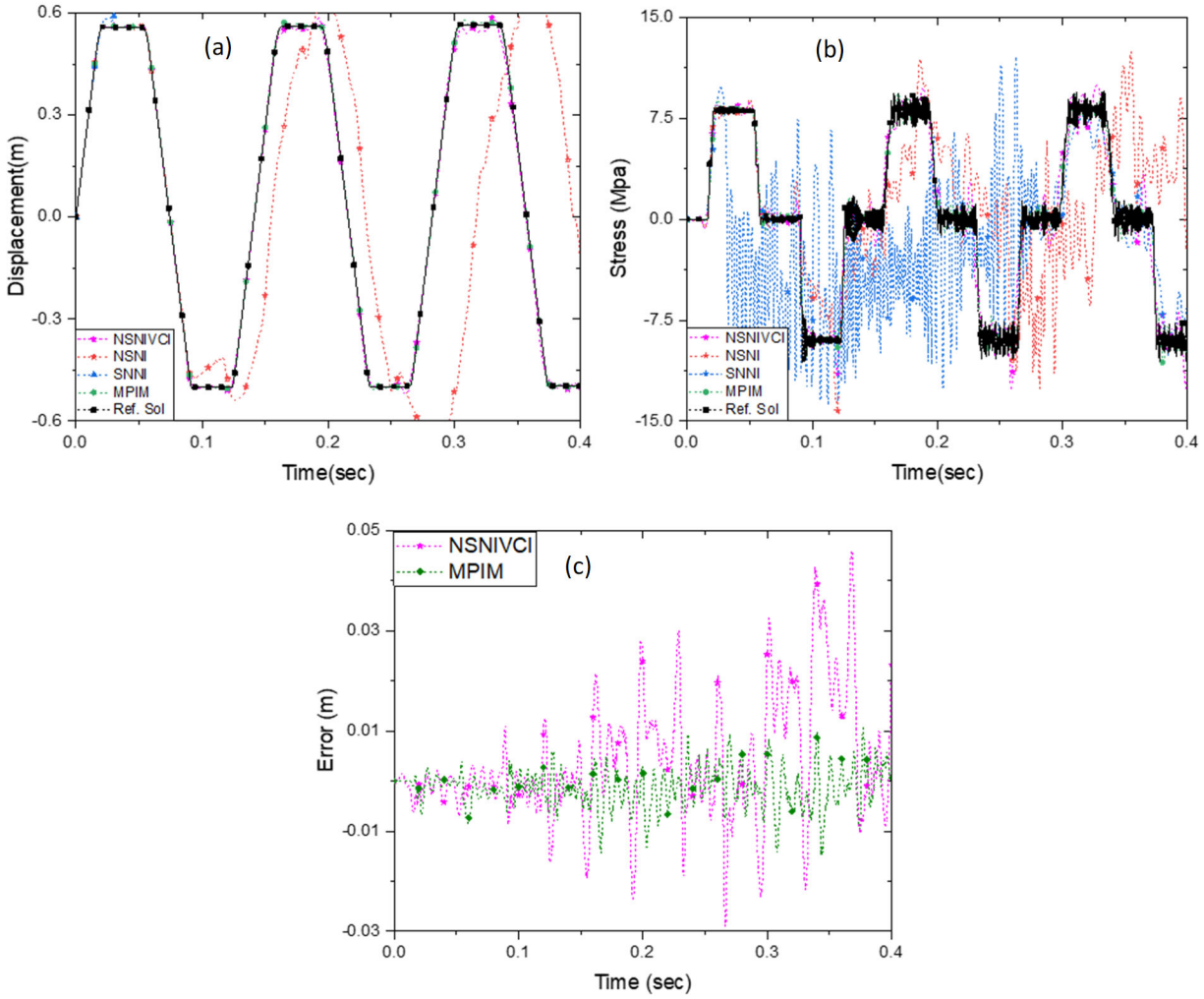

Figure 5. Time history of (a) displacement, (b) stress, and (c) displacement error at the middle node of the bar

3.1.2.3. Cantilever Beam Under a Shear Load

A cantilever beam in Figure 6 subjected to a shear force is employed to investigate the convergence of the MPIM. A normalized support size 2.0 is considered and the elastic material properties are Young's modulus = 1.0 and Poisson's ratio = 0.3. From Figure 7, it is observed that DNI and SNNI perform well, with a convergence rate near 2.0, when the uniform discretization is used; however, they lose convergence when a non-uniform discretization is used. On the other hand, 5-point Gauss integration provides good accuracy but a low convergence rate. The MPIM shows good accuracy and a convergence rate of 2.0 in both uniform and non-uniform discretization.

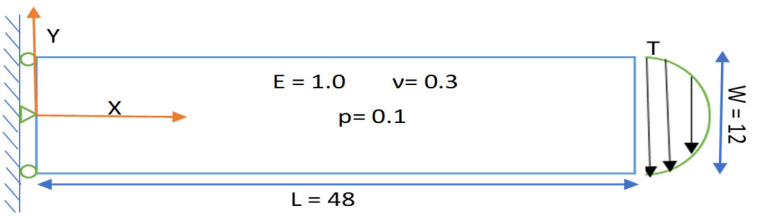

Figure 6. Schematic of cantilever beam under a shear load

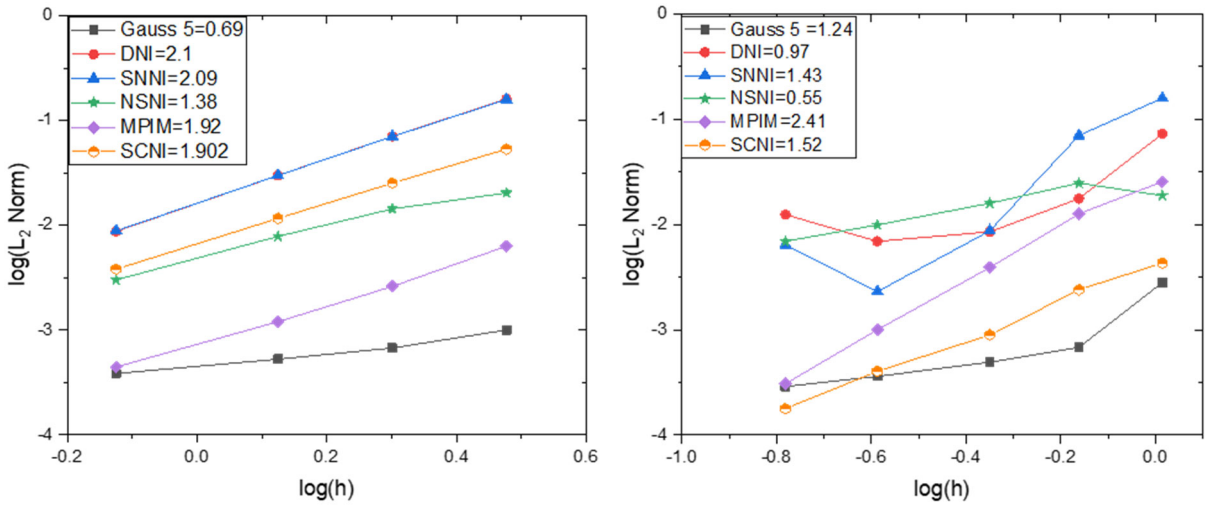

(a) (b)

Figure 7. Convergence study using (a) uniform and (b) non-uniform discretization

3.1.2.4. Taylor Bar Impact Problem

A classical Taylor bar impact problem (Taylor 1948) is employed to investigate the performance of the MPIM in the 3D dynamic impact problem. An aluminum bar impacts a rigid frictionless wall with an initial velocity of 373 m/s. Its material properties of the aluminum bar are given as follows: Youngs modulus (E) = 78.2 GPa, Poisson's ratio = 0.3, density = 2700 kg/m^3, and yield stress (σ_y) = 290 MPa. The initial height and diameter of the aluminum cylinder are 23.46 cm and 0.782 cm, respectively. The updated Lagrangian framework is adopted and the cylinder is discretized by 25000 nodes with a normalized support size of 1.65. Linear basis and cubic B-spline kernel function are used in the RK approximation. A J2 plasticity model with isotropic hardening is considered for the aluminum and the yield function is given as

$$f(s,\bar{e}_p) = \|s\| - \sqrt{\frac{2}{3}}\sigma_y(1+125\bar{e}_p)^{0.1} \qquad (5)$$

where s is the deviatoric portion of the Cauchy stress, $\bar{e}_p$ is the equivalent plastic strain, and σ_y is the yield stress. The numerical solutions of the MPIM alongside MSNNI and NSNI+VCI are

shown in Figure 8, where the color map indicates the plastic strain. The overall deformation of all three integration schemes has a good agreement with the experimental measurements. Moreover, the smooth contour and the nodal connectivity (gridlines) demonstrate that the solutions are stable without spurious oscillation modes.

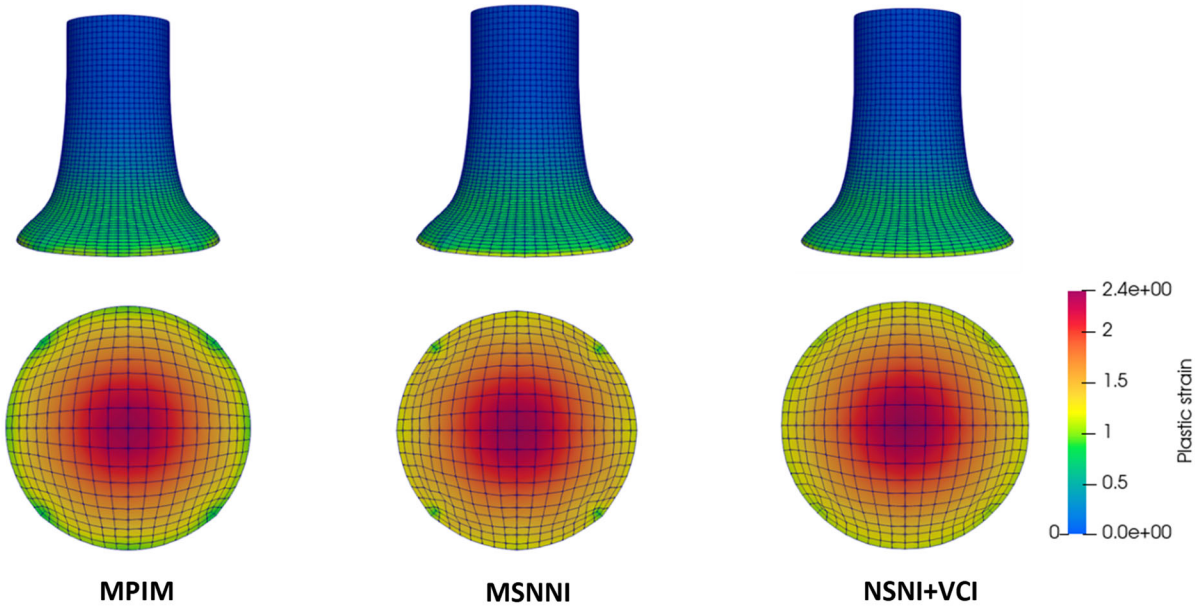

Figure 8. Plastic strain contour of the Taylor impact problem

3.1.2.5. Elastic Ball Collision with Cuboid Target

To assess the performance of the MPIM in the elastic impact problem, a spherical ball with a velocity of 80 m/s (equivalent to 60% of the elastic wave speed) colliding with the stationary target is studied. The radius of the ball is 27.25 mm and the length of the cuboid in each direction is 200 mm. Both objects are elastic with the same material properties: Youngs Modulus (E) = 40 MPa, Poisson's ratio = 0.3, and density = 2000 kg/m^3. The semi-Lagrangian framework with the kernel contact algorithm (Chi et al., 2015) is employed and a normalized support size of 1.50 is considered. The discretization of the problem is shown in Figure 9.

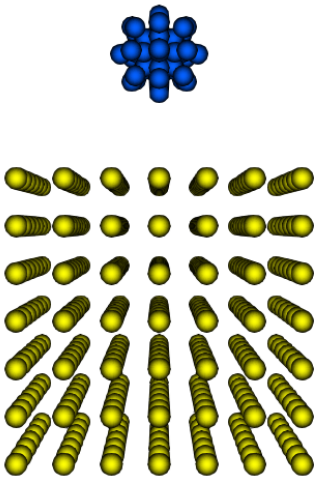

Figure 9. Discretization of the spherical ball and cuboid target

The simulation solutions in Figure 10 show that the deformation of the spherical ball and cuboid target in the MPIM solution remains symmetric and stable throughout the simulation, whereas the solutions of MSNNI and DNI are stable initially but become unsymmetrical and oscillatory at a later time. To further investigate, the linear momentum and total energy of the system are examined in Figure 11(a) and (b). It is observed that the linear momentum and total energy are conserved in the MPIM and DNI solutions whereas they are steady at initial instances but diverge at a later time in the MSNNI and NSNI solutions. The histories of the mean velocities of the spherical ball cuboid target are shown in Figure 11(c) and (d) using several different integration schemes. It can be seen that the numerical solutions obtained by the MPIM show better accuracy and stability in comparison with those obtained by commonly-used nodal integration methods.

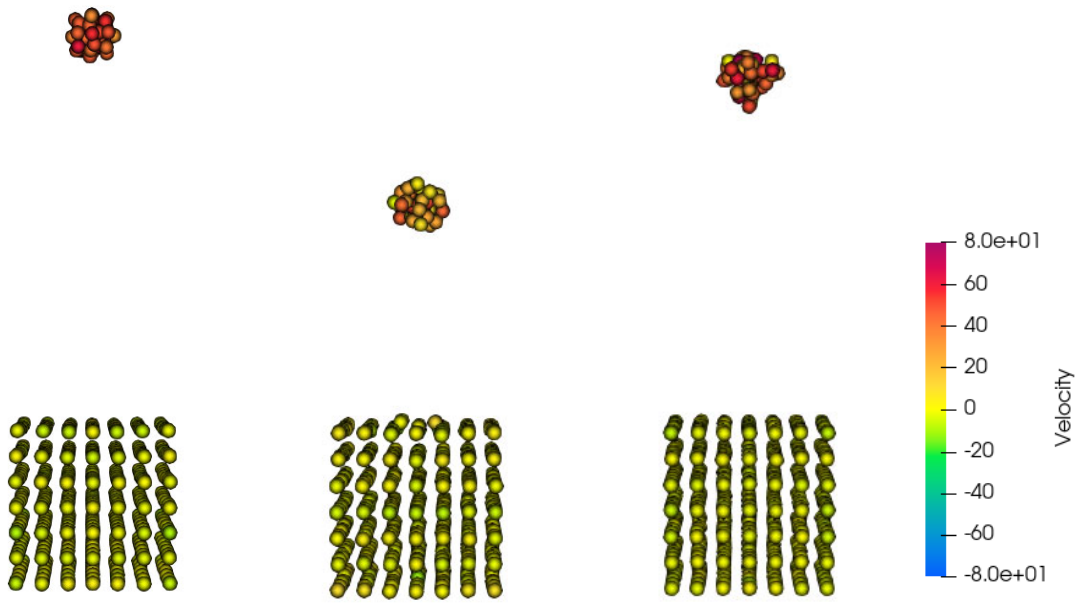

(a) MPIM (b) DNI (c) MSNNI

Figure 10. Deformation of the spherical ball and cuboid target at 0.012 second after collision

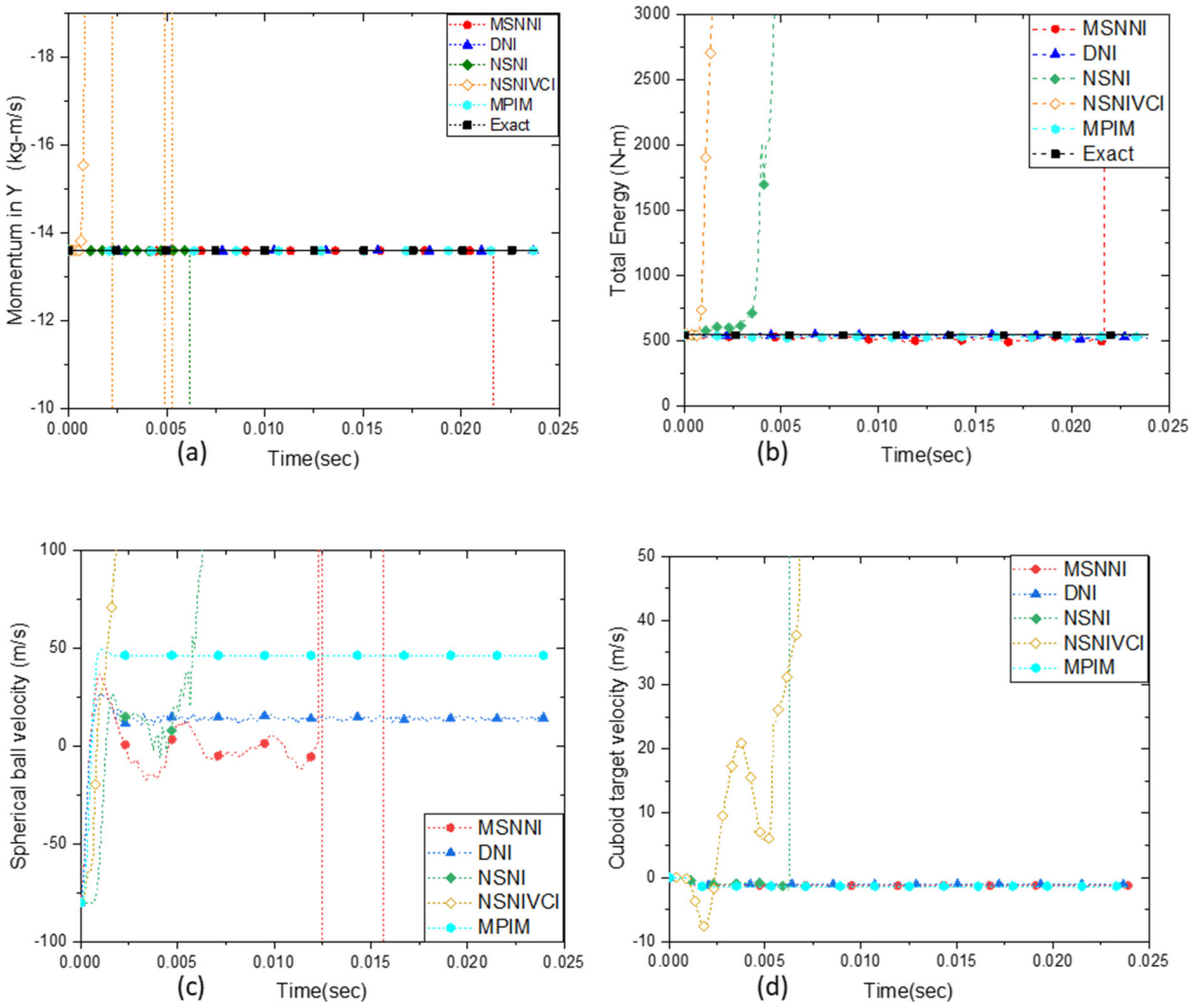

Figure 11. Time history of (a) linear momentum, (b) total energy, (c) spherical ball mean velocity, and (d) cuboid target mean velocity

3.2. Soil Constitutive Model Improvement

3.2.1. Develop Material Constant Calibration Strategy

As the three-invariant soil model has several parameters, a rigorous strategy is necessary to fit the material parameters. The procedure developed for the soil model used in this project is adapted from the procedure for the original Sandia GeoModel. That procedure is described in Fossum and Brannon, 2004.

Linear elastic material properties can be derived first. These can be calculated from the elastic straight-line portion of triaxial tests. It is important to be able to measure lateral expansion to obtain Poisson's ratio. The failure surface can be determined using a least-square fit of a set of triaxial test. Since the failure surface now contains a unified tension-shear surface, at least one tension test

must be performed for cohesive soils. For non-cohesive soils, the tensile strength can be considered to be zero or very close. It is recommended to perform at least 3 triaxial compression tests to ensure accuracy.

The ratio of triaxial extension to compression strength ψ, can be fit with a triaxial extension experiment. If that is unavailable, the Mohr-Coulomb approximation can be used.

$$\psi = \frac{1}{1 + \sqrt{3}\,(M\,(C - MI_1)[(C - MI_1)^2 - (C - M\Xi)^2]^{-\frac{1}{2}}} \tag{6}$$

The cap parameters can be fit using a hydrostatic compression test, or very high yield strength triaxial tests. These need to be fit simultaneously. Currently, a trial-and-error approach is used and produces reasonable values quickly. The evolution parameters are fit next. These are fit, again with a trial and error procedure, to capture the plastic portion of the curve. Finally, the rate-dependent parameters are fit to higher strain-rate tests.

As an example, a clay tested by Xu and coworkers (Xu, et al, 2018) is selected to verify the fitting procedure. The fit parameters are shown in Table 1. The fits to the data from these parameters are shown in Figure 12. Although the authors refer to the data as stress-strain, there is considerable inhomogeneity in the softening regime as a shear band forms. The model captures this formation as well, as shown in Figure 13.

Table 1. Material parameters for the modified GeoModel fit to clay from Xu et al., 2018

$E = 9733.3$ kPa	$a_t = 225.0$	$\gamma_C = 1.0$
$\nu = 0.3$	$a_c = 225.0$	$\gamma_C^g = 1.0$
$\psi = 1.0$	$a_s = 225.0$	$\gamma_\Xi = 1.0$
$\hat{R} = 4.0$	$C_{max} = 39.8$ kPa	$C_0 = 39.7$ kPa
$S = 0.0$	$C_{max}^g = 39.8$ kPa	$C_0^g = 39.7$ kPa
κ_0 = -1000.0 kPa	$\Xi_{max} = 249.2$ kPa	$\Xi_0 = 248.7$ kPa
$M = 0.1598$	$C_{res} = 15.0$ kPa	$n_0 = 0.5$
$M_g = 0.1$	$C_{res}^g = 15.0$ kPa	$n_0^* = 0.5$
$q_1 = 2.0$	$\Xi_{res} = 93.9$ kPa	$\tau = 0.3$

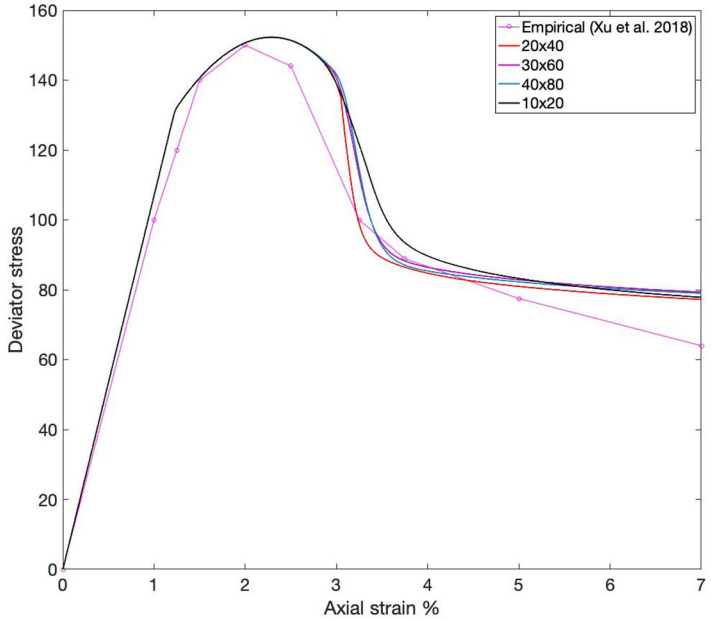

Figure 12. Fit of stress-strain data to tests from Xu et al., 2018

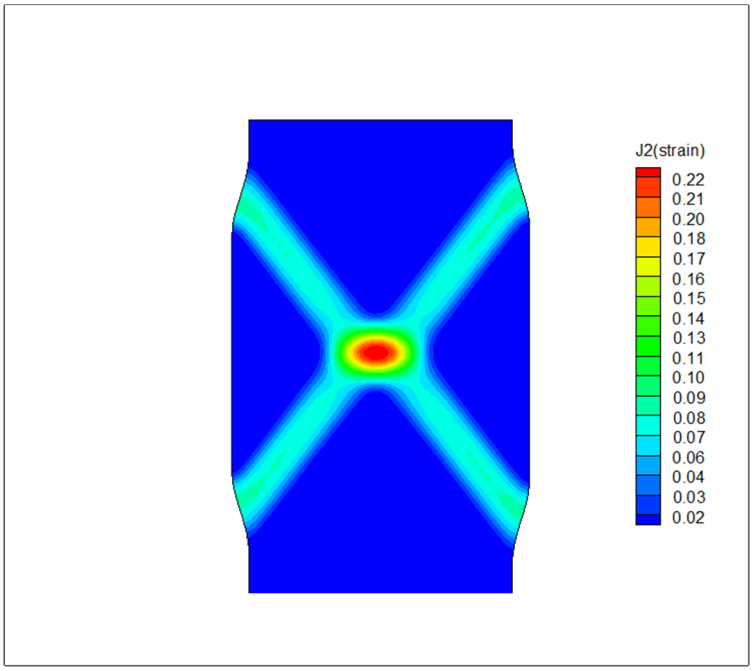

Figure 13. Equivalent plastic strain of clay sample after triaxial compression, showing conjugate shear bands

3.2.2. Sensitivity Analysis for the Three-Invariant Soil Model

To enhance the efficiency of parameter calibration for the soil model, a Sobol variance-based sensitivity analysis (Saltelli et al., 2010) is performed to investigate the effect of each parameter on the simulation results. The general procedure of the sensitivity analysis is as follows: First, a set of input parameters is defined based on the problem of interest. A sequence of perturbed parameter sets is generated based on a sampling method with a defined range of variation and a probability distribution. The sequence of parameter sampling sets, referred to as input, is transferred as the inputs into the designated numerical model for analysis. The numerical results, referred to as output, are extracted for the sensitivity analysis. In the Sobol sensitivity analysis, the first-order and total Sobol sensitivity indices for each parameter can be obtained and the predominant parameters can be identified.

The first-order index S_i is a direct variance-based measure. It indicates the contribution to the output variance of the main effect of X_i and measures the effect of varying X_i alone. The total effect index S_{Ti} takes into account the contribution to the output variance of X_i, including all variance caused by its interactions with any other input parameters. The first-order index and the total effect index can be calculated as follows.

$$S_i = \frac{V_{Xi}(E_{X\sim i}(Y \mid X_i))}{V(Y)} \tag{7}$$

$$S_{Ti} = \frac{E_{X\sim i}(V_{Xi}(Y \mid X_{\sim i}))}{V(Y)} = 1 - \frac{V_{X\sim i}(E_{Xi}(Y \mid X_{\sim i}))}{V(Y)} \tag{8}$$

where X and Y are the input and output datasets, respectively, $V(Y)$ represents the variance of the output, $X\sim i$ is the input except the i^{th} input, E_{Xi} is the effect of X_i, and $E_{X\sim i}$ is the effect of $X\sim i$. Many Monte Carlo estimators are available for both indices. The following estimators are employed in this study:

$$V_{Xi}(E_{X\sim i}(Y \mid X_i)) = \frac{1}{n}\sum_{j=1}^{n} f(A)_j (f(A_B^{(i)})_j - f(B)_j) \tag{9}$$

$$E_{X\sim i}(V_{Xi}(Y \mid X_{\sim i})) = \frac{1}{2n}\sum_{j=1}^{n} (f(A)_j - f(A_B^{(i)})_j)^2 \tag{10}$$

Above for a k dimensional sampling Sobol sequence, $\boldsymbol{A}$ and $\boldsymbol{B}$ are two $n\times k$ variance matrices generated by the Monte Carlo method. $f(\boldsymbol{A})_j$ and $f(\boldsymbol{B})_j$ represent the outputs for the j^{th} sample in $\boldsymbol{A}$ and $\boldsymbol{B}$, respectively, and $f(\boldsymbol{A_B}^{(i)})_j$ represents the output for the j^{th} sample by replacing the i^{th} column of $\boldsymbol{A}$ with the i^{th} column of $\boldsymbol{B}$. The details can be found in Saltelli et al., 2010.

In this project, two scenarios are designed to determine critical parameters for the constitutive model. To expedite the analysis, the three-invariant soil model is converted into a user-defined subroutine for ABAQUS, a finite element analysis software. The numerical simulations are obtained by using ABAQUS.

3.2.2.1 Sensitivity Analysis for Triaxial Compression Test

The schematic of the setting is shown in Figure 14. The baseline parameters for the model are given in Table 2. The parameters vary +/-5% in the sampling process in the sensitivity analysis. One hundred samples in total are randomly generated and 3100 models are run in total to extract the outputs. The sensitivity indices of the maximum stress are calculated and shown in Figure 15 and Figure 16. As can be seen in both Figures, only 4 parameters have significant effects on the maximum stress in the triaxial compression test. From Figure 16, it also reveals that the initial yield stress κ_0 has the most significant effect on the maximum stress.

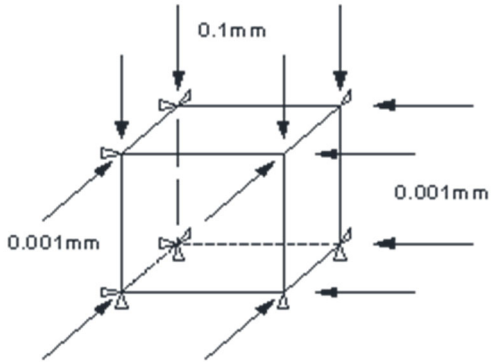

Figure 14. Schematic of triaxial compression test for sensitivity analysis

Table 2. Baseline material parameters

E=9000.0 MPa	a_t=100.0	γ^g_C=2.0
v=*0.15*	a_c=100.0	γ_Ξ=1.0
ψ=0.8	a_s=50.0	C_0=4.5
$\hat{R}$=1.5	C_{max}=5.5 MPa	C^g_0=3.0
S=0	C^g_{max}=7.0 MPa	Ξ_0=10.0
R=0	Ξ_{max}=11.0 MPa	n_0=0.2
M_g=0	C_{res}=2.0 MPa	n^*_0=0.2
κ_0=-50.0 MPa	C^g_{res}=0.5 MPa	q_1=0.1
M=0.2	Ξ_{res}=7.0 MPa	τ=*0.0*
M_g=0.05	γ_C=1.0	

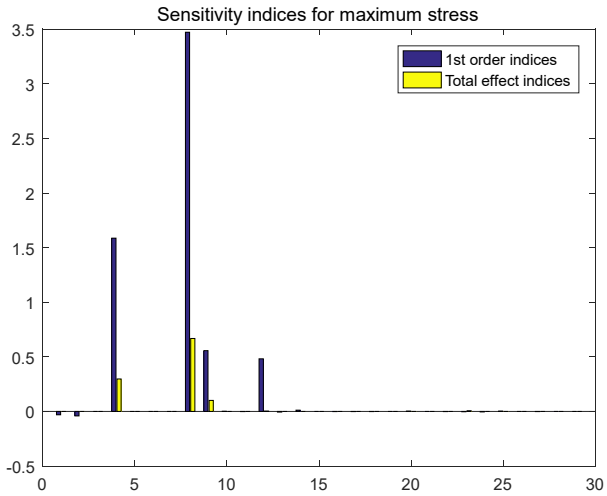

Figure 15. First-order indices and total effect indices for maximum stress in triaxial compression

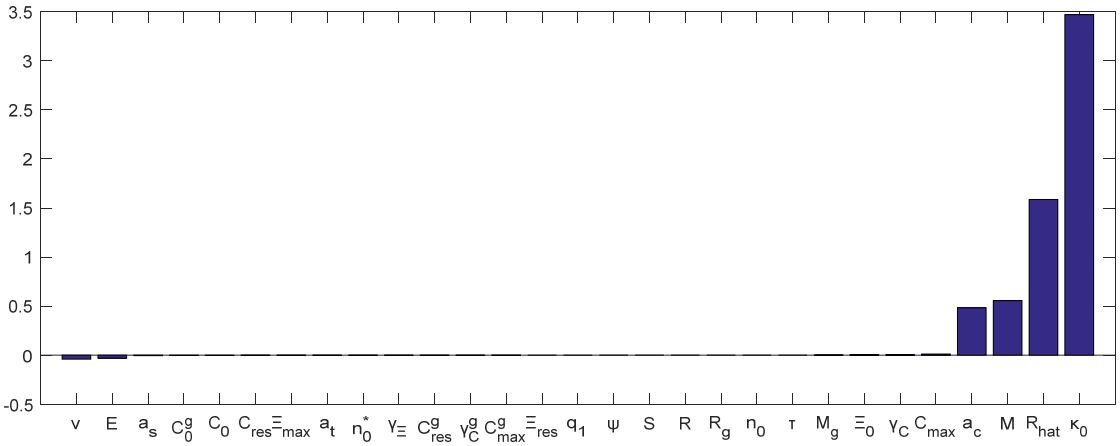

Figure 16. First-order sensitivity index ranking in the triaxial test

3.2.2.2. Sensitivity Analysis for Hertz Contact

To mimic the dominant deformation modes in the impact problem while accounting for computational efficiency, circular contact stress, extracted from the Hertz contact problem, is applied at the center of a cuboid in the quasi-static FE simulation. The finite element mesh and boundary condition are shown in Figure 17 and the contact stress distribution along the radial direction is given in Figure 18. The magnitude of the contact stress is obtained from the Hertz contact problem with the plastic effect neglected and can be expressed as $p(r) = p_0\sqrt{1-r^2/a^2}$, where a is the contact radius, E represents the elastic modulus, ν represents the Poisson's ratio, and $p_0 = 2E(a/r)/\pi(1-\nu^2)$.

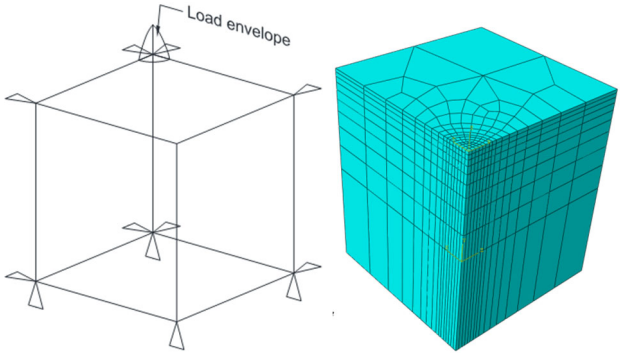

Figure 17. Schematic and finite element mesh for Hertz contact problem

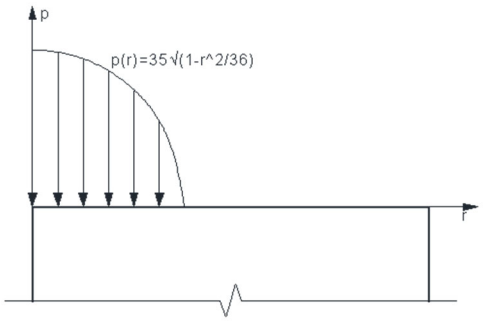

Figure 18. Contact stress distribution

To evaluate the plastic deformation and indentation depth, three measured values are selected as the output parameters: 1) maximum indentation displacement, 2) the number of yielding integration points, and 3) plastic index. The maximum indentation displacement is a direct measurement of the deformation of interest whereas counting the number of yielding integration points is aimed to evaluate the size of the plastic zone in the simulations. To further account for the level of plastic strain in the plastic zone, the plastic index is defined as follows.

$$PI = \frac{1}{nip}\sum_{i=1}^{nel}\sum_{j=1}^{nip} V_i \varepsilon_{e\ j}^{p} \tag{11}$$

where V_i is the volume of the i-th element, $\varepsilon_{e\ j}^{p}$ denotes the equivalent plastic strain at j-th integration points in the i-th element, nel is the number of elements, and nip is the number of integration points in each element. In total, 800 samples are generated as the inputs and 24800 finite element models are analyzed. The sensitivity indices for the maximum displacement, number of yielding integration points, and plastic index are given in Figures 19-24. The elastic modulus E has a predominant effect on the maximum displacement, followed by the initial shear strength C_0 and the initial yield stress κ_0. On the other hand, the initial shear strength C_0 and the shear yield surface parameter M contribute most to the plastic zone size and plastic index.

In summary, we conduct the Sobol sensitivity analysis to identify parameters that play an influential role in the three-invariant soil model, such as, the initial shear strength C_o, shear yield surface parameter M, the elastic modulus E, and the initial yield stress κ_0. This work may suggest specific experimental tests and data fitting strategies for calibration of key parameters.

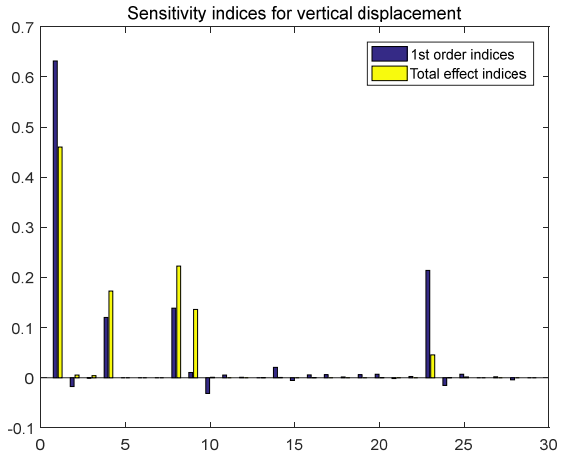

Figure 19. First-order indices and total effect indices for maximum displacement in the Hertz contact

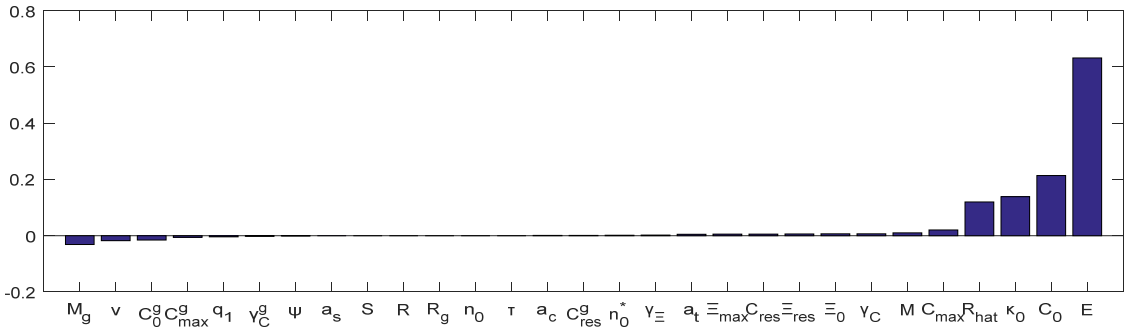

Figure 20. First-order sensitivity index ranking for maximum displacement in the Hertz contact

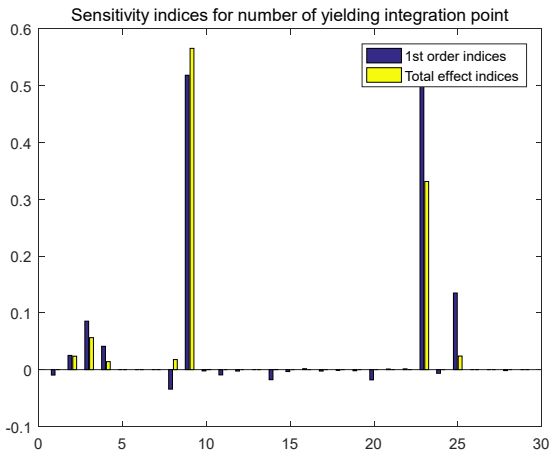

Figure 21. First-order indices and total effect indices for plastic zone size in the Hertz contact

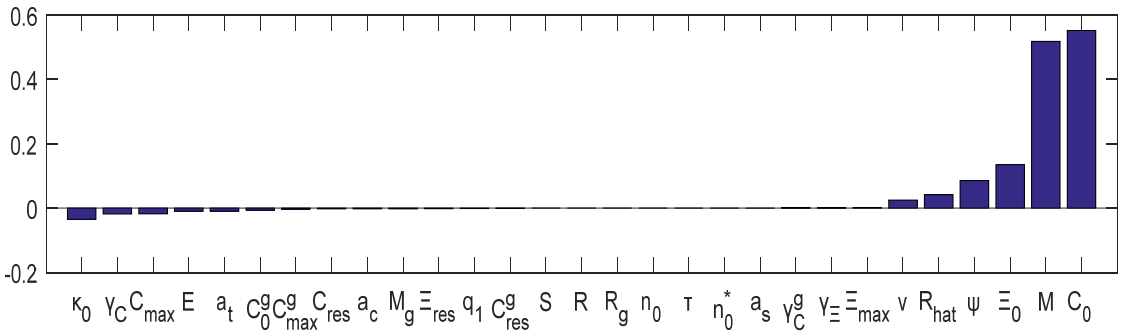

Figure 22. First-order sensitivity index ranking for plastic zone size in the Hertz contact

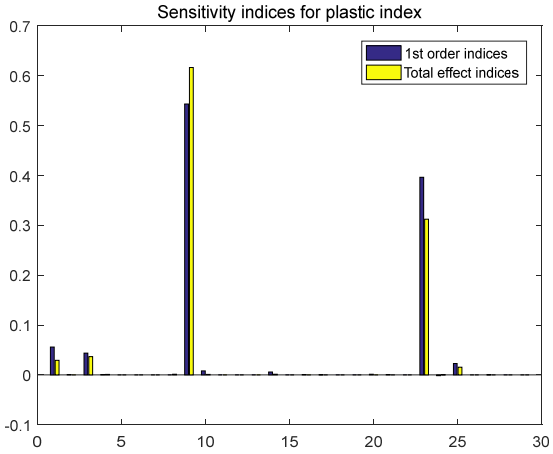

Figure 23. First-order indices and total effect indices for the plastic index in the Hertz contact

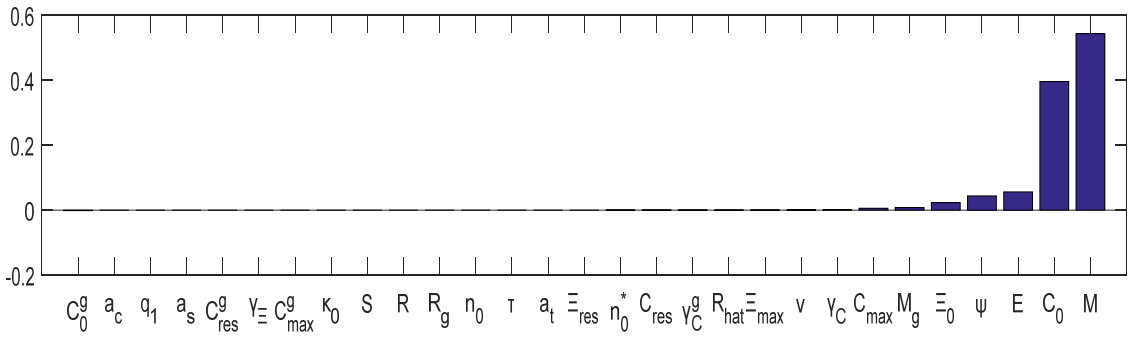

Figure 24. First-order sensitivity index ranking for the plastic index in the Hertz contact

3.2.3. Partially Saturated Soil Model

A partially saturated soil model is developed, largely following Borja and White (2012). The formulation extends Biot mixture theory for partially saturated soils. The model assumes that the air pressure remains near gauge pressure for the simulation.

The strong form of governing equation comes from the balance of linear momentum and fluid mass. The balance of momentum equation can be written

$$\nabla.\sigma + \bar{\rho}g = 0, \tag{12}$$

$$\bar{\rho} = \phi^s.\rho_s + \phi^w.\rho_w \tag{13}$$

where ϕ^s and ϕ^w are the volume fraction of solid and liquid, respectively. ρ_s is the solid mass density and ρ_w is the liquid mass density. $\bar{\rho}$ is the mixture density of porous media consist of water and solid. σ is Cauchy stress tensor and g is the gravitational acceleration.

The conservation of liquid mass equation is given as,

$$(1-\phi^s)\frac{d\psi^w}{dt} + \psi^w\,\nabla.\nu + \nabla.\mathrm{q} = 0, \tag{14}$$

$$\mathrm{q} = -k_{rw}\,K\,.\,\nabla\left(\frac{p}{\rho_w g} + y\right) \tag{15}$$

where ϕ^s is the volume fraction of soil skeleton, ψ^w is the void fraction of liquid. K is the saturated permeability, p is the liquid pressure, ν is the intrinsic velocity for liquid and the solid part which is consistent.

The boundary condition should be defined to solve the aforementioned governing equations:

$$u = \bar{u} \quad on\ \Gamma_u \tag{16}$$

$$\sigma.n = \bar{t} \quad on\ \Gamma_t \tag{17}$$

$$p = \bar{p} \quad on\ \Gamma_p \tag{18}$$

$$-n\,.\,q = \bar{q} \quad on\ \Gamma_q \tag{19}$$

Γ_u is solid displacement boundary, Γ_t depicts solid traction boundary, Γ_p is fluid pressure boundary and Γ_q demonstrates the fluid flux boundary.

The relationship between the degree of saturation and suction results from experimental study. The mathematical model of van Genuchten equation is utilized and given as,

$$\psi^w(p) = \psi_1 + (\psi_2 - \psi_1)\left[1 + \left(\frac{-p}{s_a}\right)^n\right]^{-m} \tag{20}$$

where ψ_1 is the residual water retention, ψ_2 is the maximum water saturation, s_a is scaling pressure, and *n* and *m* are empirical constant defining the shape of the degree of saturation-suction curve. *n* and *m* are not independent but are related by,

$$m = \frac{n-1}{n} \tag{21}$$

The water phase relative permeability is defined as,

$$K_{rw}(\theta) = \theta^{\frac{1}{2}}\left[1 - \left(1 - \theta^{\frac{1}{m}}\right)^m\right]^2, \tag{22}$$

$$\theta = \frac{\psi^w - \psi_1}{\psi_2 - \psi_1} \tag{23}$$

After deriving a weak form and temporal and spatial discretization, the matrix equations can be obtained as

$$r\left(\delta^k_{n+1}\right) = \begin{bmatrix} r^k_{1_{n+1}} \\ r^k_{2_{n+1}} \end{bmatrix} = \begin{bmatrix} F_{EXT} - F_{INT}\left(\underline{d}^k_{n+1}\right) - G\underline{p}^k_{n+1} \\ G^*_{EXT} - G^T\underline{d}^k_{n+1} - (M + \alpha\Delta t\phi)\underline{p}^k_{n+1} \end{bmatrix} \tag{24}$$

where

$$F_{INT}\left(\underline{d}\right) = \int_{\Omega^e} B^{e^T}\{\sigma'\}^e \; d\Omega$$

$$G^e = -\int_{\Omega^e} H^{e^T} \psi^w \, N_p^e \; d\Omega$$

$$F_{EXT}^e = \int_{\Gamma_u^e} N^{e^T} \bar{t} \; d\Gamma + \int_{\Omega} N^{e^T} \overline{\rho} g \; d\Omega$$

$$M^e = -\int_{\Omega^e} N_p^{e^T} (1 - \phi^s) \frac{d\psi^w}{dp} N_p^e \; d\Omega$$

$$\phi^e = -\int_{\Omega^e} B_p^{e^T} \left(\frac{k_{rw} K}{\rho_w g} \right) B_p^e \; d\Omega$$

$$G_{EXT}^e = -\int_{\Gamma_q^e} N_p^{e^T} \overline{q}^e \; d\Gamma + \int_{\Omega^e} B_p^{e^T} (k_{rw} K) \begin{Bmatrix} 0 \\ 1 \\ 0 \end{Bmatrix} d\Omega$$

where $\underline{d}$ is the nodal displacement vector and p is the nodal pore water pressure. The matrix N^e is the shape function vector for the displacement, H^e is a vector containing the gradients of shape functions. The vector $N^e{}_p$ is a vector of the shape functions for the pore pressure, which may be distinct from the shape functions for the displacement, and $B^e{}_p$ is a matrix of the gradients.

The effective, or constitutive, stress σ' is used to determine the solid deformation. This is defined as

$$\sigma' = \sigma + B \, (\psi_w p_w + \psi_a p_a) \mathbf{1} \qquad (25)$$

where and **1** is the second-order identity tensor and B is the Biot coefficient, a material parameter.

3.2.3.1. Foundation Loading on Linear Elastic Clay

The response of a footing load on the linear elastic clay is analyzed using the model mentioned above. Because of the symmetry, only half of the domain is considered. The results are obtained for both saturated and unsaturated soil domain by changing the level of the water surface. The schematic is shown in Figure 25. The load increases linearly to a maximum of 100 kN over 100 days and is then maintained.

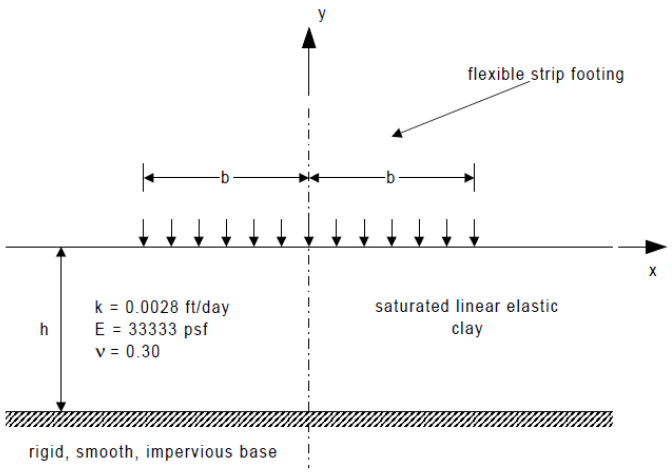

Figure 25. Schematic of a footing load on the linear elastic clay (Gibson 1970)

In the saturated case, the pore water pressure increases when the surface load is applied; then the excess pore water pressure dissipates from the media, shown in Figures 26 and 28. As a result of the dissipation of pore water pressure, there is a settlement as depicted in Figures 27 and 29. In the unsaturated case, the pore water pressure is positive at the middle of the left edge and it decreases since the sample is not saturated and no peak of water pressure is observed as shown in Figures 28 and 32.

Table 3. Property values for the linear elastic clay

Description	**Properties**	**Value**
Shear Modulus	μ	**20000 KPa**
Lamé's first parameter	λ	**80000 KPa**
Scaling Pressure (van Genuchten)	S_a	**10 KPa**
Porosity	**n**	**0.5**
Intrinsic Permeability	**K**	**5E-05 m/s**
Coefficient (van Genuchten)	**m**	**0.5**
Coefficient (van Genuchten)	**n**	**2**

Both saturated and unsaturated versions of the model are tested. The results for the saturated case are shown in Figures 26-29. Figure 26 shows the pore water pressure at the end of the

simulation, while Figure 27 shows the vertical displacement at the same time. Figures 28 and 29 show the variation in time of pore pressure and displacement at nodes along the centerline, respectively. Displacement is shown for the node at the surface, while pore pressure is illustrated for the node 5 m below the surface.

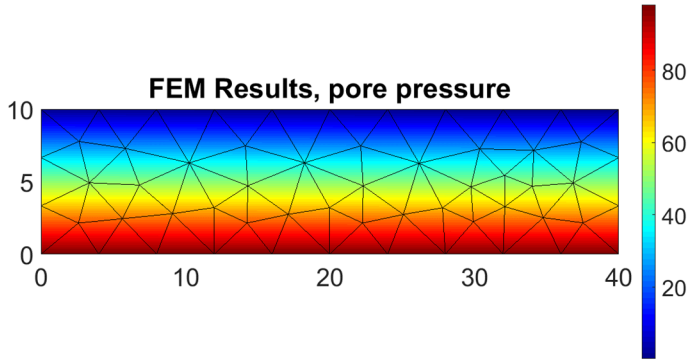

Figure 26. Pore water pressure for the saturated case

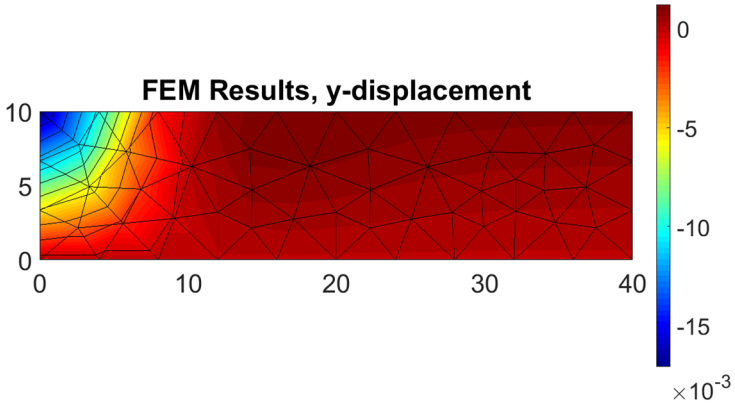

Figure 27. Vertical displacement for the saturated case

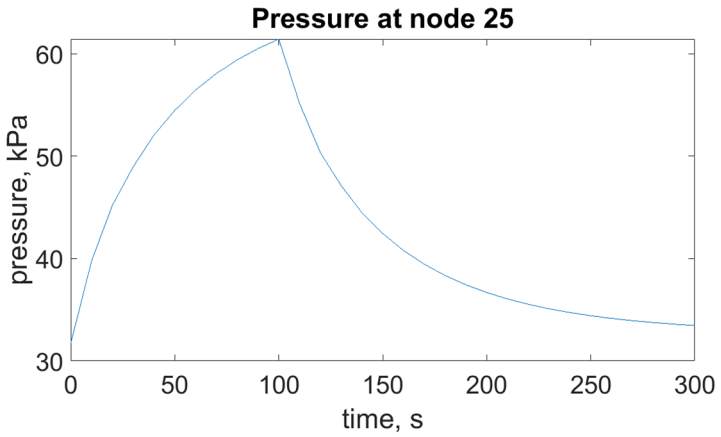

Figure 28. Pressure at the middle of the left edge for the saturated case

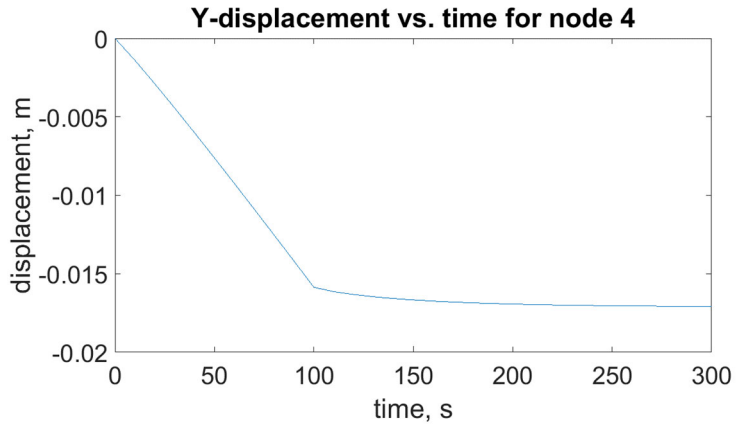

Figure 29. Displacement at the middle of the left edge for the saturated case

Figures 30-32 show results for the unsaturated case. The loading is the same as for the saturated case, but the water table is lowered to 3 m below the surface of the water. The vertical displacement and pore pressure at the end of the simulation are shown in Figures 30 and 31, respectively. The water level the water pressure is negative for the unsaturated case, which demonstrates the effects of suction pressure. The vertical displacement and pore pressure for nodes directly under the loading are shown in Figures 32 and 33, respectively. As in the saturated case, displacement is shown for the node at the surface, while pore pressure is illustrated for the node 5 m below the surface. The properties of the material are presented in Table 2.

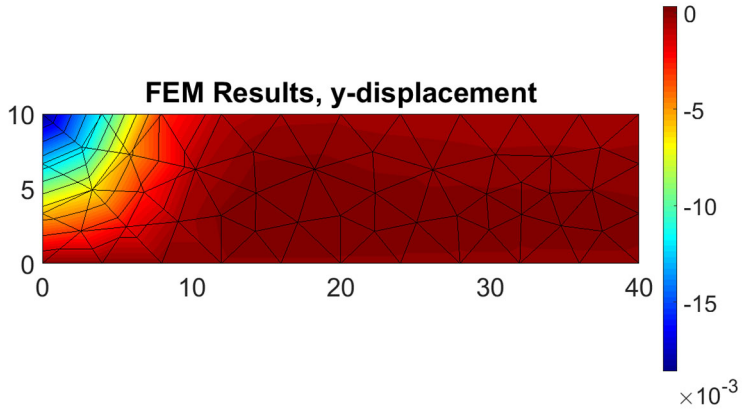

Figure 30. Vertical displacement for the unsaturated case

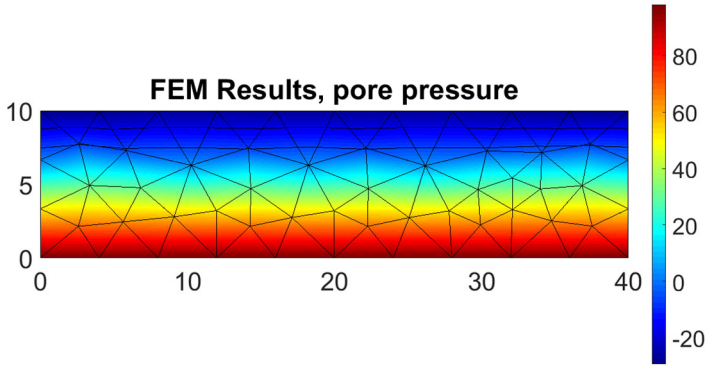

Figure 31. Pore pressure for the unsaturated case

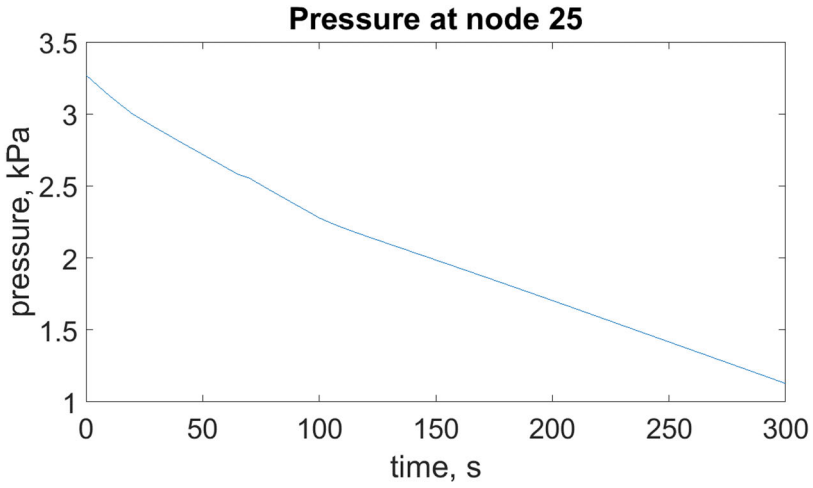

Figure 32. Pore pressure at the middle of the left edge for the unsaturated case

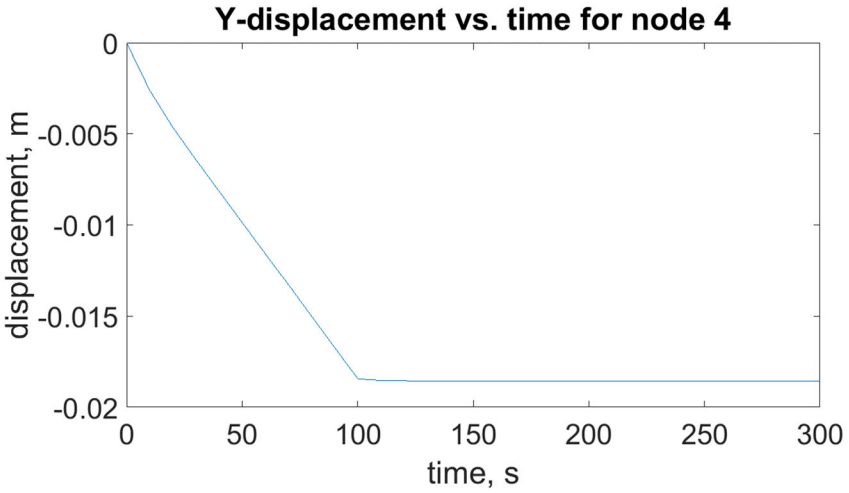

Figure 33. Displacement at the middle of the left edge for the unsaturated case

3.2.4. Algorithm Improvement and Verification

The partially saturated soil model has been implemented. Steady-state models have been verified and match the literature. However, currently, the material consolidates too quickly, as shown in Figure 34. A benchmark problem is chosen from the analytical solution developed by Gibson (1970). The geometry of the problem is given in Figure 25 and because of the symmetry of the problem, only half of the geometry is considered. The properties of the material are given in Table 3. Surface loading is applied using a linear ramp function for the first 0.05 day. To verify the saturated formulation the vertical settlement at the middle of the foundation is considered, the results are demonstrated in Figure 34.

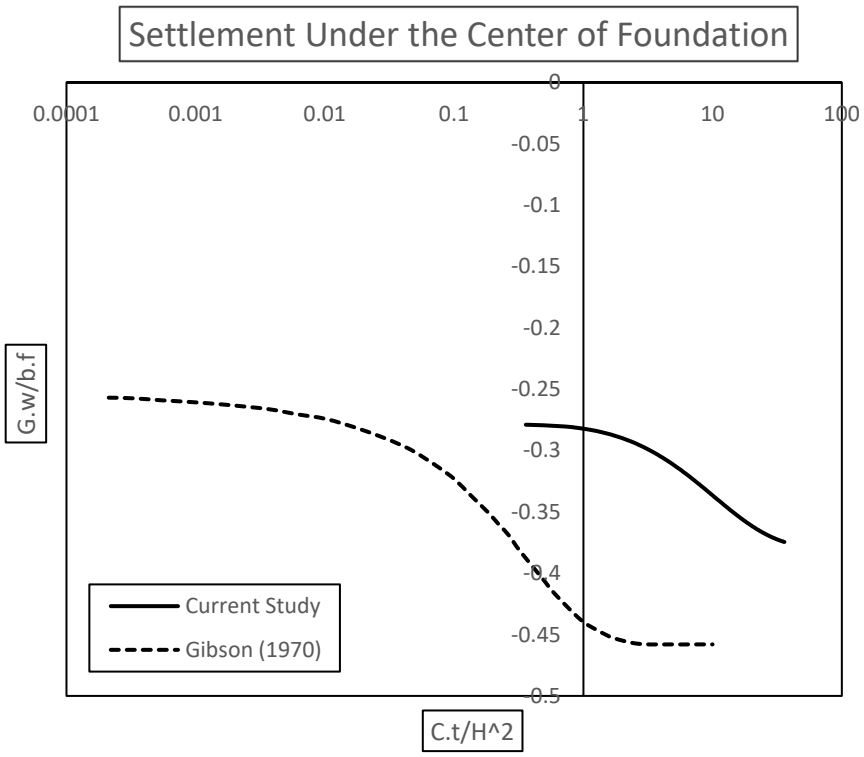

Figure 34. Benchmark comparison with Gibson (1970) showing the settlement under the center of the foundation

3.2.5. Incorporation into Meshfree Code

The soil plasticity model has been incorporated into the meshfree code. The implementation has been verified, as shown in Figure 35. Small differences arise in that the finite element simulation is quasistatic, while the meshfree simulation is dynamic. At slow loading rates, though, the results are very similar.

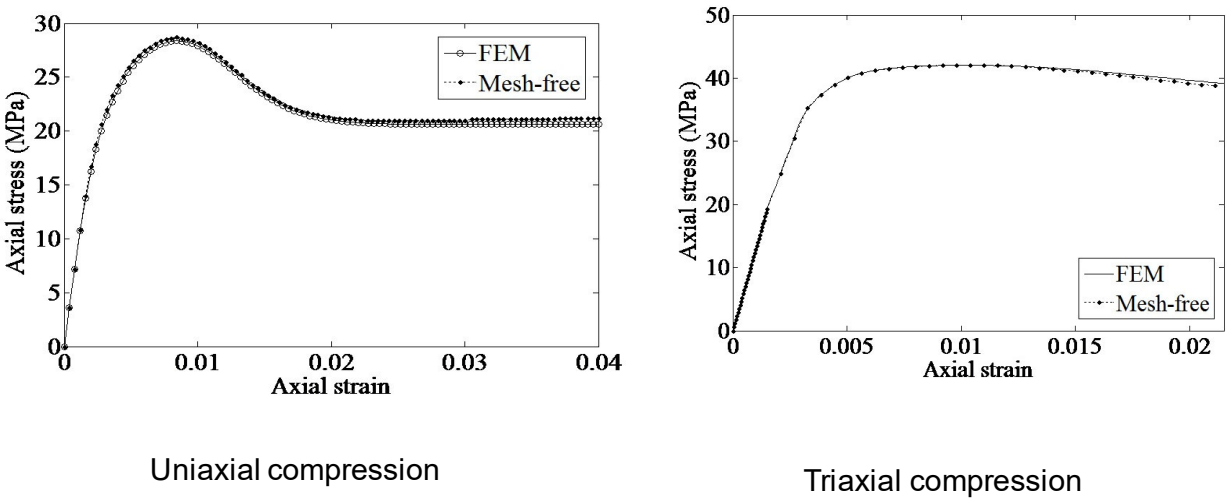

Figure 35. Verification between the meshfree and finite element implementations of the model

3.3. Soil Tests, Penetration Tests, and Validation

3.3.1. Soil Tests for Calibration Soil Mechanical Properties

The silica sand (natural grain) from U.S. Silica Company is first selected as the granular material for tests and validations. The mechanical properties of silica sand under dry conditions were determined in the previous reporting year, including density determination, specific gravity determination by pycnometer, and the grain size analysis. In this reporting year, the properties of silica sand under the fully saturated condition were obtained using the following laboratory tests.

3.3.1.1. Degree of Saturation and Water Content Determination

The saturation ratio of soil is defined as the ratio of the volume of water to the volume of voids. From the density and specific gravity of the silica sand, the volume of voids can be determined as reported. The volume of water is obtained by water content determination and is defined as:

$$\omega(\%) = \frac{M_2 - M_3}{M_3 - M_1} \times 100 \qquad (26)$$

where M_1 is the mass of the soil container, M_2 is the combined mass of the wet sand and the container, and M_3 is the combined mass of the dry sand and the container. The tests follow the procedure in ASTM D-2216, Laboratory Determination of Water (Moisture) Content of Soil and Rock by Mass. Three wet sand samples are prepared for soil properties determination followed by triaxial tests. The saturation ratio as well as friction angle and maximum stress of three samples used in the experiments are given in Tables 4-6.

Table 4. Properties of Sample #1

Test No.	Degree of Saturation	Friction Angle (°)	Maximum Stress (kPa)
Test 1	0.92	36.34	575.59
Test 2	0.91	36.49	587.29
Test 3	0.90	36.28	570.39
Mean	0.91	36.37	577.75

Table 5. Properties of Sample #2

Test No.	Degree of Saturation	Friction Angle (°)	Maximum Stress (kPa)
Test 1	0.94	36.34	578.19
Test 2	0.95	36.31	572.47
Test 3	0.97	36.51	589.37
Mean	0.95	36.39	580.01

Table 6. Properties of Sample #3

Test No.	Degree of Saturation	Friction Angle (°)	Maximum Stress (kPa)
Test 1	0.98	37.48	679.06
Test 2	0.95	37.31	662.42
Test 3	0.96	37.23	653.84
Mean	0.96	37.34	665.11

3.3.1.2. Consolidated Drained Triaxial Test (CD)

The consolidated drained triaxial test (CD) was conducted to determine the shear strength parameters of the sand sample, following the ASTM D7181-11 code. The specimen was saturated with 5-psi backpressure and stood for 24 hours to ensure the water is uniformly distributed among the sample. A 15-psi confining pressure and three deformation speeds (1%, 5%, and 10% of strain per minute) were applied to the samples. The degree of saturation was kept between 0.9 and 1. The

dimension of the cylindrical specimen has a diameter of 70.0 mm and a height of 122.9 mm by sucking the membrane on the membrane stretcher with a vacuum pump (Figure 36). Each sample is loaded with the specific strain rate until one of the following occurs: 1) the load dial decreases significantly on the specimen, 2) the load remains constant for at least four deformation dial readings, or 3) at least 15% strain is reached. The saturation ratio of each specimen is also measured after the triaxial test.

The load-displacement data are recorded directly from the experiments and can be processed to obtain the stress-strain data, given in Table 11 in Appendix, and the corresponding stress-strain curves for different loading rates and tests are shown in Figures 37-39. The friction angles can be obtained by processing the stress-strain curves and are given in Tables 4-6. Other parameters in the soil model can be calibrated from the stress-strain data using the fitting strategies described in Section 3.2.1.

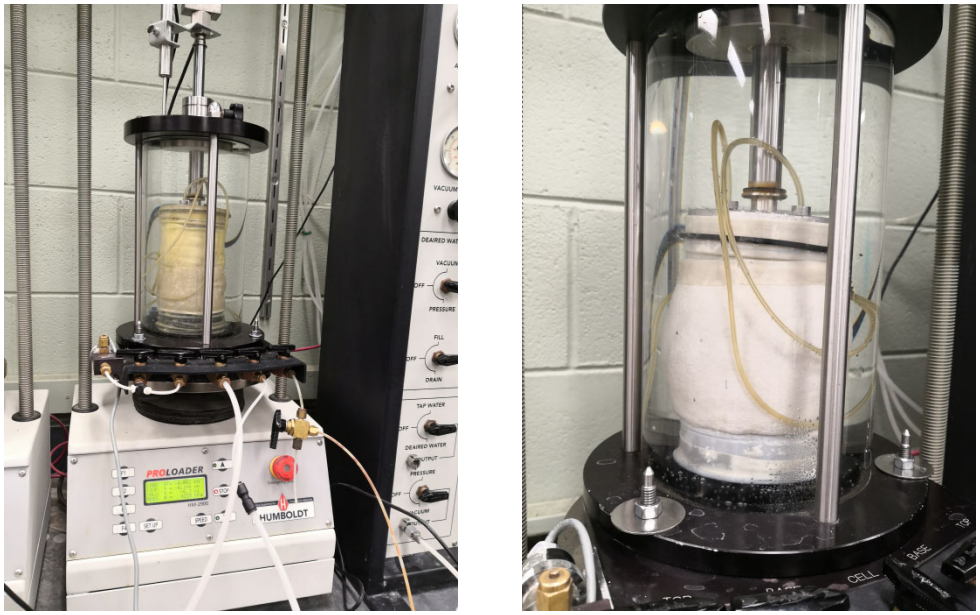

Figure 36. Triaxial test. (left) sample before loading and (right) sample after loading

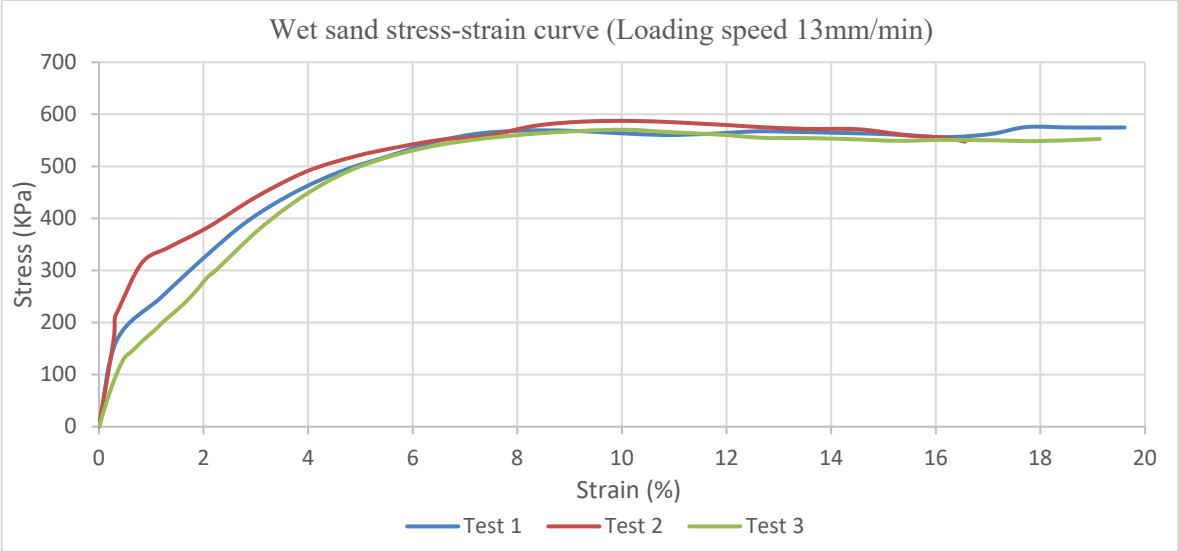

Figure 37. Stress-strain curves of the consolidated drained triaxial test (CD) for Sample #1 with a loading rate of 13 mm/min

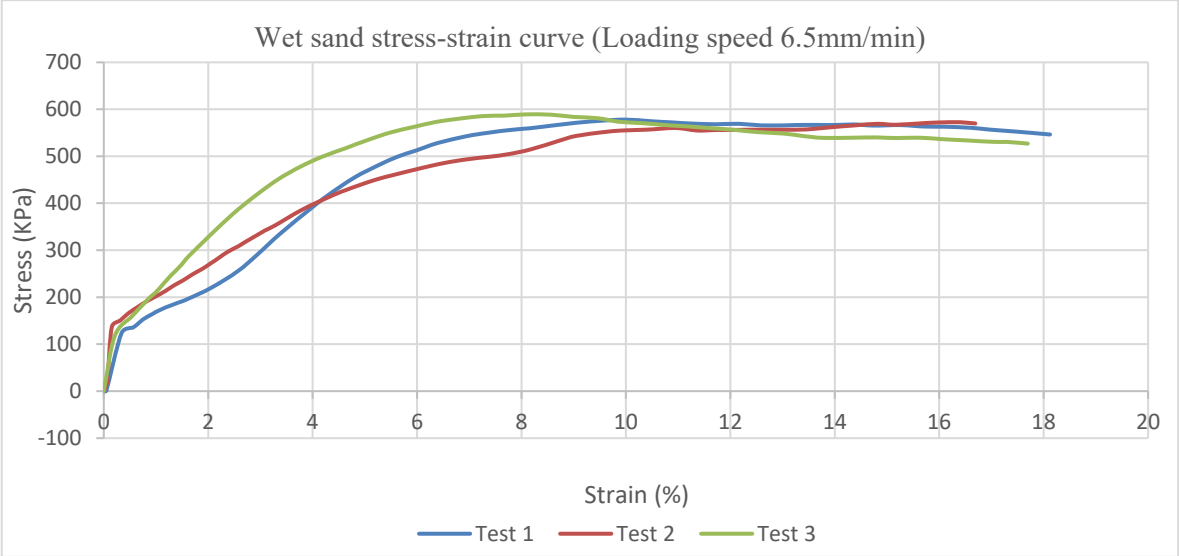

Figure 38. Stress-strain curves of the consolidated drained triaxial test (CD) for Sample #2 with a loading rate of 6.5 mm/min

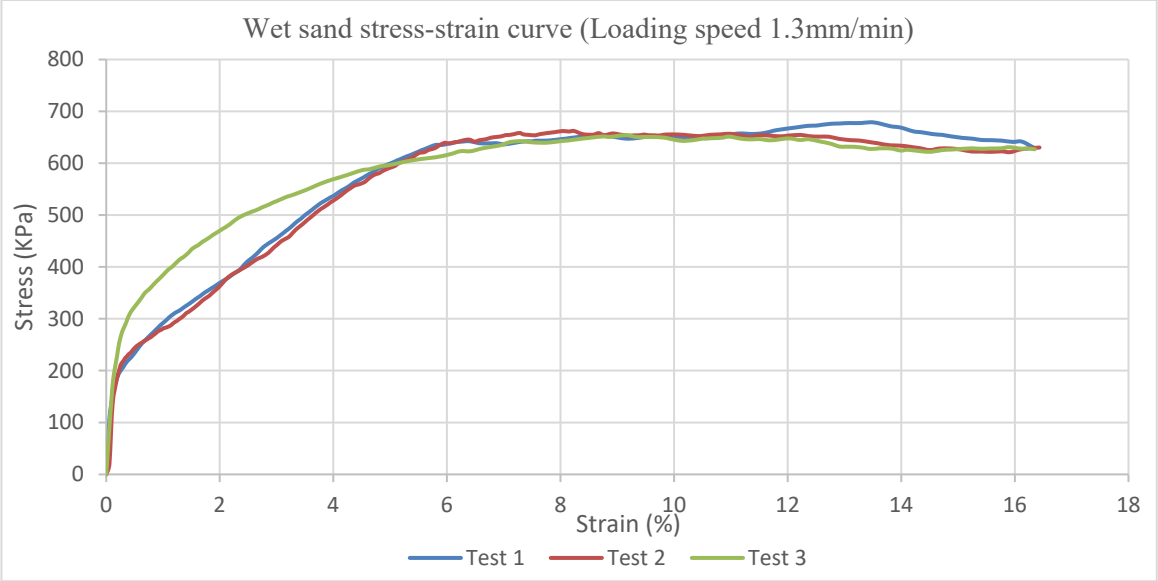

Figure 39. Stress-strain curves of the consolidated drained triaxial test (CD) for Sample #3 with a loading rate of 1.3 mm/min

3.3.2. Apparatus for Penetration Test

A penetration testing apparatus is built and placed in the High-Bay Structures Laboratory at the UIC (Figure 40). The main goals of building the apparatus are to provide penetration testing data consistent with the soil testing data, validate the simulation results, and guide the modification of the current model. The system has a steel frame of 10' height and a 40" ×40" base and can hold a soil container of 2' height and 1.5' length ×1.5' width at the bottom. A pneumatic gun mounted at the center of the upper frame is designed to launch a steel ball of 1" diameter to a speed up to 120 m/s. The precise speed of the projectile is measured by a chronograph. Due to the impact of COVID-19, the completion date of the apparatus is delayed. Some test runs are conducted to verify the design of the system, including shooting the steel ball up to 50 m/s, measuring the projectile speed, capturing the penetration images, and measuring the depth of penetration. The system will achieve its full designed capability after a little tuning and be ready to conduct penetration tests for various soil conditions.

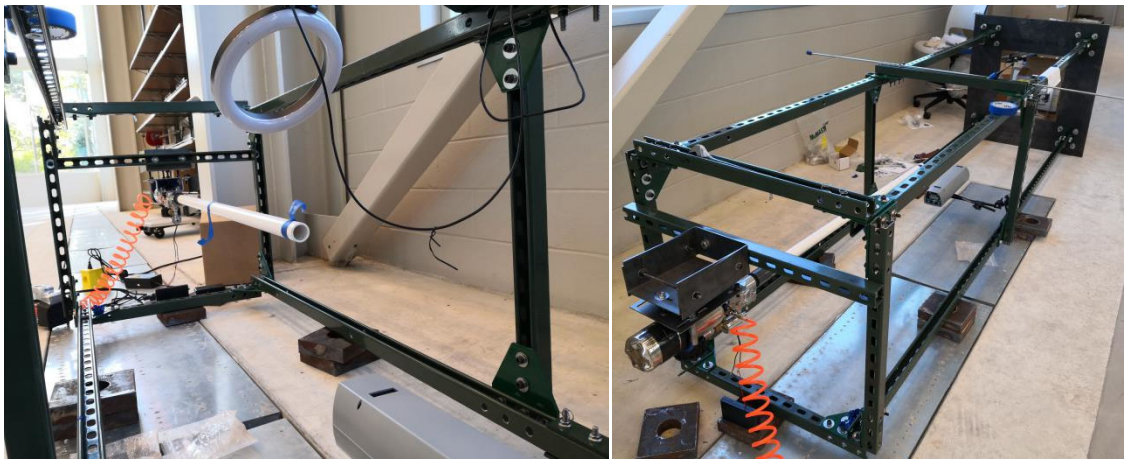

Figure 40. Apparatus for penetration test

3.3.3. Validation of Projectile Penetrating into Soil

The experimental data in Hankins et al. (2006) is considered to validate the developed meshfree code for modeling penetration into soil. An ogive bullet of length 41.66 mm and radius 2.083 mm made up of aluminum is projected with various velocities into the coarse sand. Several impact velocities ranging from 24 m/s to 170 m/s are simulated. The semi-Lagrangian framework is considered with a normalized support size of 1.50 and the MPIM described in Section 3.1.1 is employed. Nearly 75100 nodes are used for the simulation, with an averaged nodal distance of 2.0 mm for both projectile and soil. This discretization keeps a good balance between accuracy and computational efficiency. The soil grain is modeled by using the Drucker-Prager with damage model and the aluminum bullet is modeled as linear elastic. The elastic material properties are adapted from the data reported in Hankins et al. (2006) and the plastic and damage parameters are calibrated using the penetration data for the impact velocity of 170 m/s. The calibrated material parameters are given in Tables 7 and 8. The numerical setup for this simulation is shown in Figure 41.

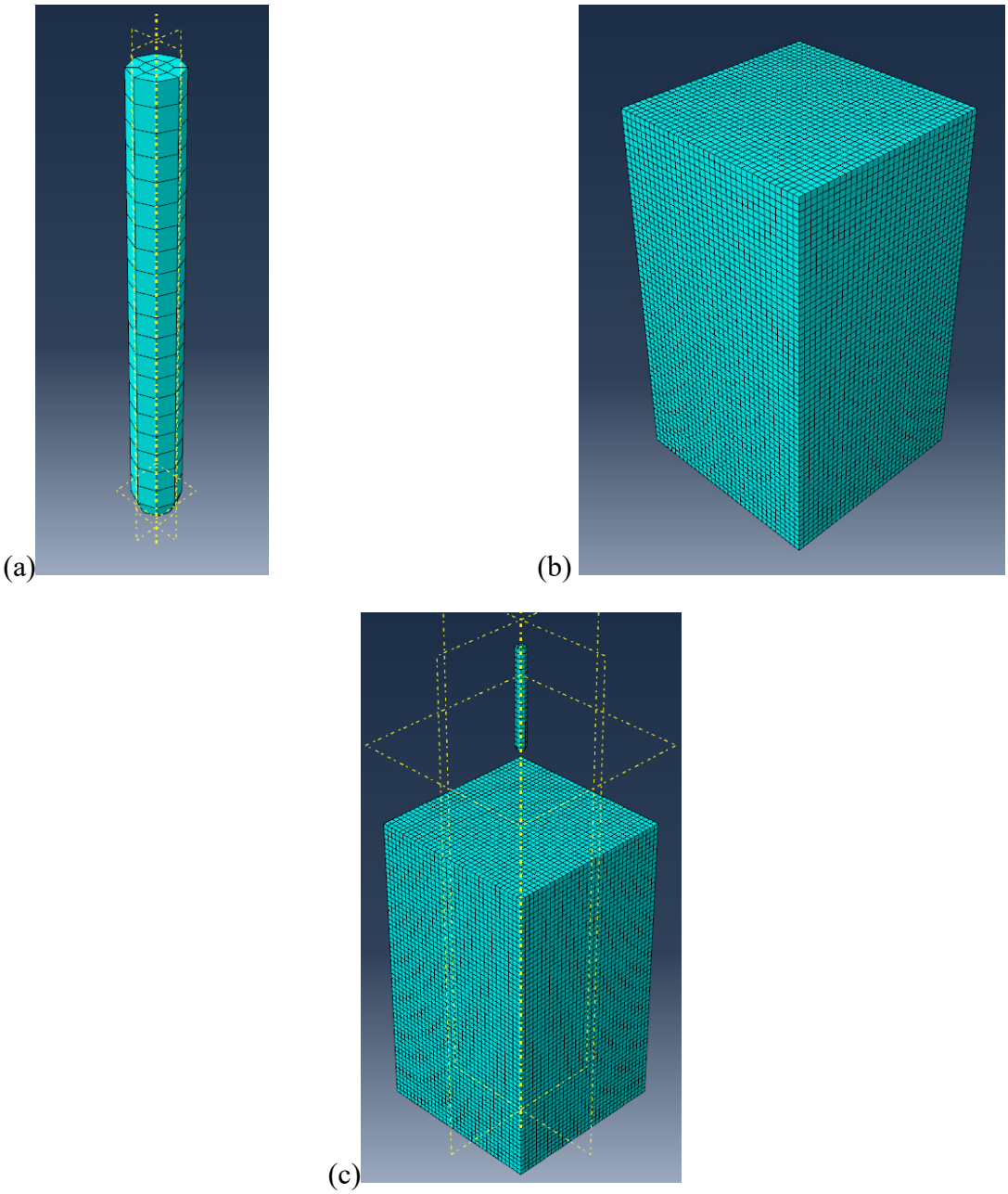

Figure 41. (a) bullet projectile mesh configuration, (b) soil mesh configuration, and (c) initial configuration in the numerical model

Table 7. Drucker-Prager parameters and properties

Drucker-Prager soil properties	
Young's modulus ($\boldsymbol{E}$)	$1.5 \times 10^7 \frac{N}{m^2}$
Poisson's ratio ($\boldsymbol{\nu}$)	0.32
Friction Parameter ($\boldsymbol{\beta}$)	0.1
Hardening	$0.0 \frac{N}{m^2}$
Cohesion strength ($\boldsymbol{\alpha}$)	0.0
First parameter for damage accumulation function	0.05
Second parameter for damage accumulation function	1.0
Density ($\boldsymbol{\rho}$)	$1450 \frac{kg}{m^3}$
Mass-proportional damping coefficient	0.05

Table 8. Material properties of the bullet

Linear Elastic Material	
Young's modulus ($\boldsymbol{E}$)	$7.82 \times 10^{10} \frac{N}{m^2}$
Poisson's ratio ($\boldsymbol{\nu}$)	0.32
Density ($\boldsymbol{\rho}$)	$2800 \frac{kg}{m^3}$
Mass proportional damping coefficient	0.05

Figure 42 shows the simulation results for the projectile velocity of 170 m/s. The color contour in Figure 42 indicates the level of damage (1 as 100% damaged). The numerical solutions using the MPIM remain stable throughout the simulation time and the soil deformation in the simulation agrees with the experimental data in Hankins et al. (2006). Several impact velocities are simulated to attain the numerical prediction and form a trend line. The resulted trend line is validated with the experimental data and shown in Figure 43. The numerical prediction qualitatively captures the tendency of the experimental data.

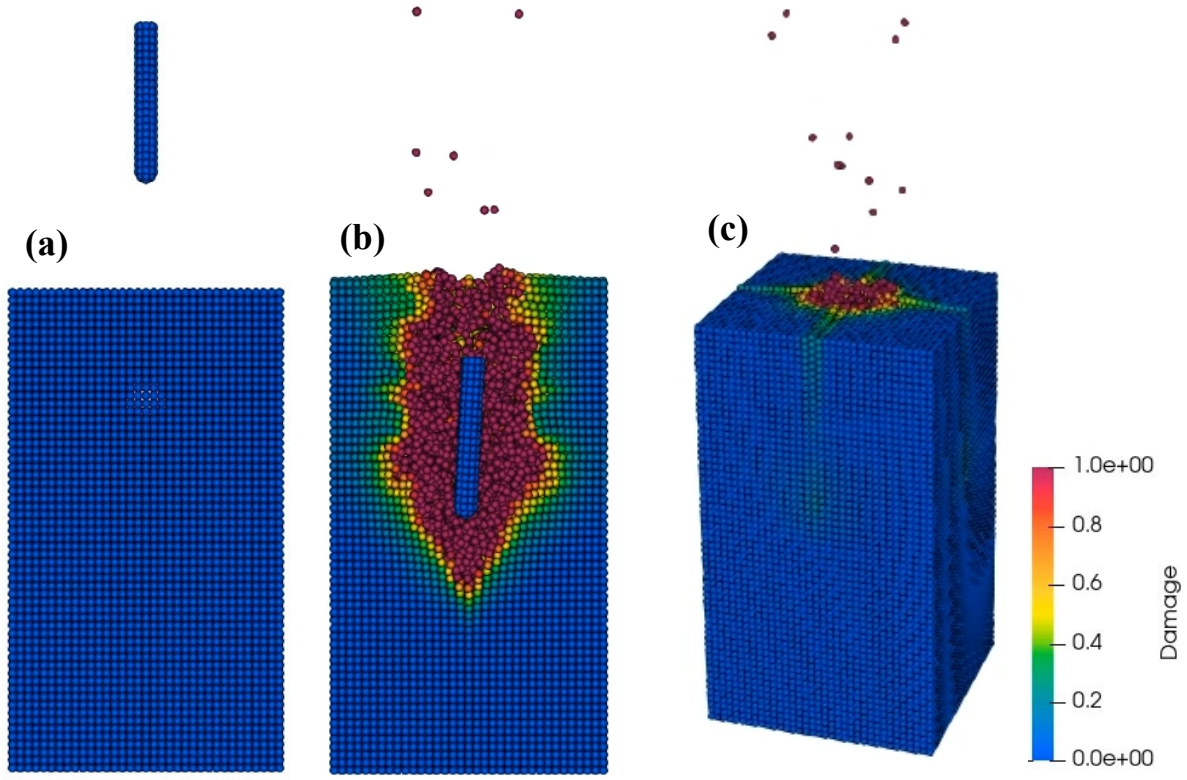

Figure 42. Penetration simulation results. (a) initial configuration, (b) sectional view of deformation of soil after bullet penetration, and (c) oblique view of deformation of soil after bullet penetration

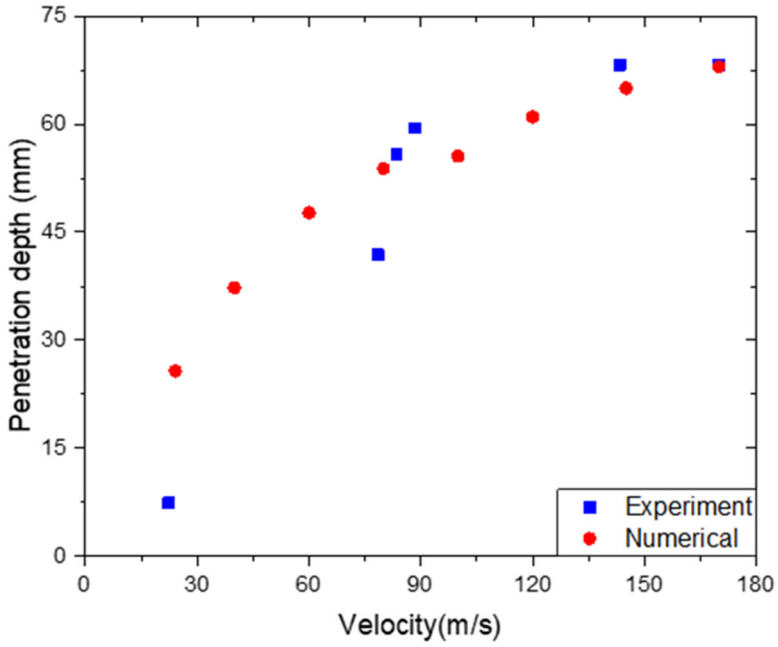

Figure 43. Penetration depth of various impact velocities from experiments and numerical solutions

4. References

Borja, R.I and White J.A. Conservation Laws for Coupled Hydro-Mechanical Processes in Unsaturated Porous Media: Theory and Implementation. LLNL Book 424150, 2012.

Cerone, P., and Dragomir, S. S. (2000). Midpoint-type Rules from an Inequalities Point of View. *Handbook of Analytic-Computational Methods in Applied Mathematics, CRC Press, 135–200.*

Chen, J.S., Wu, C.T., Yoon, S., and You, Y., 2001. A Stabilized Conforming Nodal Integration for Galerkin Meshfree Methods. *International Journal for Numerical Methods in Engineering*, 50, 435-466.

Chen, J.S., Wu, C.T., Yoon, S., and You, Y., 2002. Nonlinear Version of Stabilized Conforming Nodal Integration for Galerkin Meshfree Methods, *International Journal for Numerical Methods in Engineering*, 53, 2587-2615.

Chen, J.S., W. Hu, M. Puso, Y. Wu, and X. Zhang, Strain Smoothing for Stabilization and Regularization of Galerkin Meshfree Method. Lecture Notes in Computational Science and Engineering, 2006. **57**: p. 57-76.

Chen, J.S., M. Hillman, and M. Ruter, An arbitrary order variationally consistent integration for Galerkin meshfree methods. International Journal for Numerical Methods in Engineering, 2013. **95**(5): p. 387-418.

Chen, J.S., Hillman, M., and Chi, S.W., "Meshfree Methods: Progress Made after 20 Years," Journal of Engineering Mechanics, 2017, 2017. 143(4): p. 04017001.

Chi, S.W., Lee, C.H., Chen, J.S., and Guan, P.C., A level set enhanced natural kernel contact algorithm for impact and penetration modeling, International Journal for Numerical Methods in Engineering, 2015. 102(3):839-866.

Fossum, A. F. and Brannon, R. M.: The Sandia GeoModel: theory and user's guide. SAND report, Sandia National Laboratories, 2004. Hankins, M. D., Stoltz, B. C., Torres, K. L. & Jones, S. E. (2006). "Penetration of a coarse sand target by rigid projectiles". *WIT Transactions on The Built Environment, Vol 87, 2006 WIT Press*.

Hillman, M., Chen, J.S., Chi, S.W. (2014). "Stabilized and variationally consistent nodal integration for meshfree modeling of impact problems". *Computational Particle Mechanics 1 (3), 245-256.*

Hillman, M. and Chen, J. S. (2016). "An accelerated, convergent, and stable nodal integration in Galerkin meshfree methods for linear and nonlinear mechanics". *Int. J. Numer. Methods Eng. 107 (7): 603–630*Khan, M., Mechanics of projectile penetration into non-cohesive soil targets. Vol. 13. 2015. 28-39.

Mahdavi, A., Chi, S.W., and Atif, M.M., "A two-field semi-Lagrangian reproducing kernel model for impact and penetration simulation into geo-materials," Computational Particle Mechanics, 7, p. 351–364 (2020)

Saltelli, Andrea et al. Variance Based Sensitivity Analysis of Model Output. Design and Estimator for the Total Sensitivity Index." Computer physics communications 181.2 (2010): 259–270. Web.

Taylor, Geoffrey Ingram. "The Use of Flat-Ended Projectiles for Determining Dynamic Yield Stress I. Theoretical Considerations." Proceedings of the Royal Society of London. Series A. Mathematical and Physical Sciences 194, no. 1038 (1948): 289-99.

Xu, Y., Wu, S., Williams, D. J., and Serati, M.: Determination of peak and ultimate shear strength parameters of compacted clay. *Engineering geology*, 243:160–167, 2018

Yu. K. Bivin, (2005). "Penetration of Rigid Bodies into Loose and Layered Media". *Institute for Problems in Mechanics*.

Yu, Weiping, and James P Blanchard. An Elastic-Plastic Indentation Model and Its Solutions. Journal of materials research 11.9 (1996): 2358–2367.

5. Appendix

Table 9. Stress-strain results of the consolidated drained triaxial test (CD) for Sample #1 with a loading rate of 13 mm/min

Test 1		Test 2		Test 3	
Strain	Stress (kPa)	Strain	Stress (kPa)	Strain	Stress (kPa)
0.0000	103.3524	0.0000	103.3524	0.0000	103.3524
0.3393	269.2175	0.2823	272.0772	0.2352	178.2257
1.1961	352.6700	0.3019	312.3736	0.4614	231.5209
2.0439	431.1829	0.3767	329.5321	0.6404	249.1993
2.8535	499.2968	0.8194	417.9241	0.9138	275.7169
3.7771	555.4517	1.3279	447.5614	1.0643	288.4557
4.6713	595.4881	2.0814	486.2979	1.2246	304.3143
5.5378	623.0456	3.0041	544.5327	1.6013	337.3313
6.3946	650.0832	3.9650	593.4083	1.8739	366.1888
7.2335	665.9418	4.8975	622.7857	2.0716	390.1066
8.1375	672.1812	5.7453	640.9840	2.2693	407.0051
9.0602	671.6613	6.5639	654.7628	3.0887	484.7381
9.9268	667.2417	7.4117	662.0421	3.9552	549.4723
10.8120	663.6020	8.3442	681.5404	4.8031	595.7481
11.6973	666.2018	9.2579	689.3397	5.6599	625.1254
12.5826	670.6214	10.1993	690.6396	6.5077	644.6237
13.4491	669.3215	11.0472	687.7798	7.4020	657.3625
14.3434	667.2417	11.9886	682.8403	8.3068	665.9418
15.0594	665.1618	12.6200	678.9406	9.1823	671.4013
16.1424	659.4424	13.5509	675.3009	10.0862	673.7411
17.0561	665.6818	14.5224	674.7810	10.8682	669.3215
17.7339	678.9406	15.3792	664.1219	11.7909	664.9019
18.6094	677.9007	16.1896	658.1425	12.6672	658.4025
19.6086	678.1607	16.5566	650.8631	13.4483	657.8825
				14.3718	655.5427
				15.2945	652.4230
				16.1041	654.2428
				17.0464	653.4629
				17.9219	651.9030
				18.7974	654.7628
				19.1367	656.0627

Table 10. Stress-strain results of the consolidated drained triaxial test (CD) for Sample #2 with a loading rate of 6.5 mm/min

Test 1		Test 2		Test 3	
Strain	Stress (kPa)	Strain	Stress (kPa)	Strain	Stress (kPa)
0.0000	103.3524	0.0000	103.3524	0.0000	103.3524
0.2075	220.6019	0.0464	104.3923	0.0659	124.9305
0.5370	262.7181	0.3385	227.1013	0.1505	239.5801
0.8666	301.1946	0.5647	239.3202	0.3108	253.6189
0.9984	314.1934	0.7535	256.2186	0.4614	268.6975
1.1489	332.9117	0.9227	267.3976	0.6404	281.9563
1.2807	349.2903	1.0919	277.2768	0.8007	293.3953
1.4695	370.3484	1.2620	285.0761	0.9894	304.8343
1.6298	391.1465	1.4402	292.3554	1.1774	316.5332
2.0342	435.0826	1.6103	299.8947	1.3377	328.2322
2.4679	480.3185	2.0618	323.8126	1.5167	339.1512
2.8910	518.5350	2.5614	358.3895	1.6859	351.3701
3.3336	554.1518	2.9382	394.0062	1.8747	363.0690
3.7762	581.9693	3.3710	438.2023	2.0439	375.2879
4.1725	601.9875	3.9552	491.4975	2.2132	388.0268
4.6428	621.2258	4.2945	520.6149	2.3735	400.2457
5.0382	637.6043	4.8031	558.5714	2.5712	411.6847
5.4809	653.7229	5.2644	584.5691	2.6469	416.8842
5.9430	666.2018	5.6127	601.9875	2.8259	428.8431
6.3662	676.6008	5.9707	615.5063	2.9951	439.5022
6.7998	683.3602	6.4036	631.8848	3.0797	445.2216
7.2425	688.8197	6.9406	645.9236	3.2685	455.6207
7.6664	690.1196	7.3832	653.9829	3.7860	489.1577
8.0903	692.7194	7.8072	659.7023	4.2945	515.9353
8.5606	691.9394	8.1554	663.0820	4.6428	532.0538
8.9943	687.2599	8.5883	668.8015	5.1611	552.0720
9.4557	684.6601	9.0309	674.5210	5.5191	562.9910
9.8511	677.1208	9.6062	679.7205	6.0651	577.8097
10.3124	674.0010	10.0016	681.5404	6.4133	586.6489

10.8308	669.3215	10.4719	678.1607	6.8657	595.7481
11.1790	666.9817	10.8674	675.5609	7.3841	602.5075
11.7437	662.3021	11.2823	672.9611	7.7225	607.4470
12.0456	659.9623	11.7152	671.6613	8.1749	618.1061
12.5256	655.0228	12.1579	672.4412	8.7063	636.0445
13.0155	651.9030	12.5915	669.3215	9.0415	646.7035
13.4020	646.4435	13.0244	669.3215	9.5688	654.7628
13.7779	642.5439	13.4296	670.3614	9.9170	658.4025
14.3434	643.0638	13.9284	669.8414	10.3784	659.9623
14.7958	643.5838	14.3621	671.1413	10.9341	663.6020
15.1814	642.2839	14.7388	668.8015	11.3580	658.4025
15.6241	643.0638	15.2563	669.8414	11.6973	659.1824
16.0480	639.9441	15.7177	666.7217	12.1489	659.7023
16.4809	637.6043	16.0757	666.4617	12.5826	659.9623
17.0553	633.9647	16.6029	664.1219	13.0342	659.9623
17.2913	633.9647	16.9520	660.2223	13.4679	660.7422
17.6957	630.3250	17.4793	655.8027	13.9105	665.1618
		18.1196	649.8232	14.3808	669.3215
				14.8145	672.4412
				15.1725	670.6214
				15.6998	674.0010
				15.9634	675.3009
				16.3963	675.8209
				16.6884	673.2211

Table 11. Stress-strain results of the consolidated drained triaxial test (CD) for Sample #3 with a loading rate of 1.3 mm/min

Test 1		Test 2		Test 3	
Strain	Stress (kPa)	Strain	Stress (kPa)	Strain	Stress (kPa)
0.0000	103.3524	0.0000	103.3524	0.0000	103.3524
0.0374	144.9487	0.0561	123.1106	0.4052	168.0866
0.0570	210.7227	0.1123	239.8401	0.4614	241.9199
0.1318	266.8777	0.1782	281.9563	0.5460	271.8172
0.2075	294.4352	0.2352	307.4340	0.6119	289.4957
0.2921	309.2539	0.2636	316.2732	0.6591	298.0749
0.3678	321.2128	0.3011	321.9927	0.6965	303.0144

0.4426	329.5321	0.3295	327.1923	0.7535	309.5139
0.5460	344.3507	0.3670	331.3519	0.7819	312.6336
0.6216	355.0098	0.3954	334.9916	0.8194	316.0133
0.6973	363.0690	0.4329	338.6312	0.8666	321.2128
0.7909	373.7281	0.4801	344.6107	0.9609	330.0520
0.8666	381.2674	0.5175	349.0303	1.0545	340.9710
0.9422	389.8466	0.5549	352.4100	1.1204	349.0303
1.0456	399.7257	0.5932	355.2697	1.2148	356.0497
1.1115	406.2251	0.6208	357.0896	1.2807	362.2891
1.2148	415.0644	0.6493	358.9094	1.4036	372.9481
1.2905	419.2240	0.6591	359.6893	1.4898	378.9276
1.3751	426.2433	0.7152	363.5890	1.5541	386.7269
1.4882	434.3026	0.7535	365.9288	1.6477	394.2662
1.5541	440.0221	0.7909	368.5285	1.7144	401.8055
1.6387	446.2615	0.8194	371.1283	1.8365	410.3848
1.7234	453.2809	0.8657	375.0280	1.9211	415.5843
1.8080	459.2604	0.9040	378.6676	1.9870	421.0438
1.8934	464.9799	0.9601	382.0473	2.0716	426.5033
1.9870	471.7393	0.9788	382.8273	2.1570	434.3026
2.0724	477.7187	1.0073	385.1670	2.2604	441.3220
2.1473	482.6583	1.0448	386.2070	2.3548	448.6013
2.2506	490.9775	1.0830	387.7668	2.4866	459.7803
2.3450	497.2170	1.1204	389.8466	2.5801	461.3402
2.4207	506.5761	1.1489	391.6665	2.6656	473.5591
2.4955	514.8954	1.1766	394.7862	2.8438	486.0380
2.5712	521.1348	1.2425	399.2058	3.0423	500.8566
2.6745	531.2739	1.2710	401.8055	3.2116	515.6753
2.7404	539.0732	1.3466	407.5250	3.3906	527.1143
2.8063	544.7927	1.4028	413.7645	3.5696	544.2727
2.9292	553.8919	1.4500	416.8842	3.7103	556.4916
2.9951	558.5714	1.5256	422.8637	3.9081	569.4905
3.1172	568.7105	1.6387	433.2627	4.0496	579.8895
3.1644	572.8702	1.7234	441.3220	4.2099	591.8484
3.2490	580.1495	1.8080	447.3015	4.2286	592.8883
3.3434	589.5087	1.8828	454.8408	4.3979	602.5075
3.4280	596.5280	1.9772	463.6800	4.5679	612.1266
3.4939	602.7675	2.0618	474.0790	4.7372	622.5257
3.5883	610.5668	2.1473	483.4382	4.8975	630.3250
3.6729	617.8461	2.2408	490.7175	5.0952	639.6841

3.7575	625.1254	2.3255	495.3971	5.2832	647.4834
3.8430	630.5850	2.4109	501.1166	5.4337	651.9030
3.9276	636.3044	2.4858	505.7962	5.6127	656.8426
4.0024	640.4641	2.5899	513.8555	5.7917	662.8221
4.0968	647.7434	2.6745	519.5749	5.9992	670.8813
4.1912	653.7229	2.7404	522.6947	6.1310	677.3807
4.2758	659.1824	2.8535	530.2340	6.2913	681.0204
4.3515	665.4218	2.9382	539.5931	6.5264	687.2599
4.4264	669.8414	3.0041	545.5726	6.6892	690.1196
4.5297	676.0809	3.0887	553.3719	6.8560	694.0192
4.6151	681.5404	3.2107	560.9112	7.0448	700.2587
4.6615	684.4001	3.2766	568.1906	7.2140	704.1583
4.7844	692.1994	3.3426	575.7299	7.3743	709.3579
4.8503	695.8391	3.4369	584.0491	7.5338	714.0374
4.9349	699.9987	3.5500	594.7082	7.7225	717.6771
5.0480	704.9383	3.6070	599.9077	7.9105	723.3966
5.1139	708.3180	3.6916	607.7070	8.0521	723.3966
5.2270	713.5175	3.7852	615.5063	8.2311	726.7763
5.2929	716.6372	3.8609	620.7058	8.4101	728.5961
5.3775	720.0169	3.9455	627.4652	8.5793	729.8960
5.4906	725.4764	4.0399	634.2246	8.7771	734.5756
5.5566	728.5961	4.1245	640.7240	8.9186	734.8356
5.6412	731.9758	4.2091	648.2634	9.1164	737.4353
5.7356	736.3954	4.2937	654.7628	9.2766	736.6554
5.8202	738.9952	4.3792	660.4823	9.4646	736.3954
5.9048	738.4752	4.4638	663.0820	9.6249	738.4752
5.9992	740.5551	4.5582	667.7616	9.8413	737.4353
6.0936	742.1149	4.6143	673.2211	10.0016	740.8150
6.1595	744.1947	4.7177	681.0204	10.1619	739.5152
6.2726	744.9747	4.8031	684.1401	10.3409	738.9952
6.3572	746.0146	4.8779	689.0797	10.5386	734.8356
6.4516	744.7147	4.9813	693.7593	10.7177	737.4353
6.5362	742.6349	5.0854	698.1789	10.8771	737.6953
6.6111	741.5950	5.1326	702.3385	11.0285	737.6953
6.7152	741.5950	5.2262	707.2781	11.2164	733.2757
6.7811	741.5950	5.3393	711.4377	11.4142	737.4353
6.8747	741.8549	5.4239	717.1572	11.5745	740.2951
6.9788	739.7751	5.5094	723.1366	11.7819	738.4752
7.0350	740.0351	5.6029	724.6965	11.9601	739.5152

7.1391	741.5950	5.6688	728.5961	12.1115	739.7751
7.2327	743.4148	5.7819	732.2358	12.3092	741.5950
7.3084	744.7147	5.8478	736.6554	12.4500	744.7147
7.4117	745.7546	5.9520	742.6349	12.6290	749.9142
7.4874	745.4946	6.0269	741.5950	12.8080	755.6337
7.5720	746.7945	6.1212	743.4148	12.9772	754.3338
7.7510	746.7945	6.1871	744.4547	13.1758	750.4342
7.9113	748.6143	6.3002	747.8344	13.3539	745.7546
8.0806	750.6941	6.3946	748.8743	13.4955	749.3943
8.2970	753.8139	6.4882	744.9747	13.6932	749.3943
8.4573	755.8937	6.5736	747.8344	13.8820	750.1742
8.6363	756.4136	6.6583	749.1343	14.0325	753.2939
8.7868	757.1936	6.7518	751.7341	14.2116	750.4342
8.9845	753.2939	6.8177	753.5539	14.4093	753.8139
9.1823	750.6941	6.9406	754.8538	14.5696	750.6941
9.3613	752.2540	7.0350	757.7135	14.7478	749.9142
9.5028	754.3338	7.0822	757.7135	14.9365	748.0944
9.6819	755.3737	7.1945	759.7933	15.1155	745.7546
9.8609	755.8937	7.2799	761.8731	15.3133	747.3145
10.0391	754.3338	7.3458	759.0134	15.4923	747.0545
10.2376	753.8139	7.4394	757.9735	15.6615	747.3145
10.3971	753.0339	7.5435	757.1936	15.8031	749.3943
10.5761	754.5938	7.6184	759.0134	15.9821	751.2141
10.7551	756.1537	7.7030	760.5733	16.1701	752.7740
10.9341	757.4535	7.8072	762.1331	16.2457	749.9142
11.1131	760.5733	7.9007	763.4330	16.4337	754.8538
11.2734	760.3133	7.9862	764.7329		
11.4426	759.7933	8.0521	765.5128		
11.6314	762.6531	8.1456	764.4729		
11.8096	767.3326	8.2311	765.7728		
12.1587	772.5322	8.3247	761.8731		
12.3377	775.3919	8.4101	759.0134		
12.4972	775.9119	8.4947	758.4934		
12.5826	777.2118	8.5793	758.4934		
12.7518	779.2916	8.6737	761.3532		
12.9121	780.0715	8.7583	757.4535		
13.0911	780.8514	8.8617	759.5334		
13.2889	780.8514	8.9276	760.8332		
13.4581	782.4113	9.0407	758.7534		

13.6184	780.0715	9.1066	757.7135		
13.8063	774.6120	9.2010	756.4136		
13.9854	772.2722	9.2856	757.1936		
14.2018	764.9929	9.3800	757.1936		
14.3621	762.9130	9.4736	758.7534		
14.5509	759.5334	9.5395	757.4535		
14.7201	757.9735	9.6623	757.1936		
14.8893	754.8538	9.7380	756.6736		
15.0781	752.2540	9.8503	758.7534		
15.2571	750.6941	10.0862	758.7534		
15.4166	748.0944	10.2555	757.1936		
15.5867	747.8344	10.4443	755.6337		
15.7657	746.7945	10.6225	757.9735		
15.9634	744.4547	10.8112	759.0134		
16.1237	744.9747	10.9805	760.3133		
16.3401	732.7558	11.1408	757.7135		
		11.3385	754.3338		
		11.4890	757.4535		
		11.6680	756.6736		
		11.8657	755.1137		
		12.0171	756.6736		
		12.2238	757.9735		
		12.3743	755.6337		
		12.5533	754.5938		
		12.7136	754.5938		
		12.9015	750.4342		
		13.1001	747.8344		
		13.2506	747.3145		
		13.4573	743.9348		
		13.5801	741.8549		
		13.7966	737.9553		
		13.9658	737.4353		
		14.1635	734.8356		
		14.3426	731.9758		
		14.5028	728.5961		
		14.6721	731.7159		
		14.8706	731.7159		
		15.0488	729.6360		
		15.2376	725.9964		

		15.4166	725.9964		
		15.5769	725.2164		
		15.7648	726.2563		
		15.9154	724.6965		
		16.0944	729.8960		
		16.2832	732.4958		
		16.4337	733.5357		